SIMULATION DEVELOPMENT OF A LARGE BORE TWO STROKE INTEGRAL COMPRESSOR ENGINE TO STUDY VARIABLE NATURAL GAS COMPOSITION EFFECTS

A Thesis

by

KELSEY DANIELLE FIESELER

Submitted to the Office of Graduate and Professional Studies of
Texas A&M University
in partial fulfillment of the requirements for the degree of

MASTER OF SCIENCE

Chair of Committee,	Timothy J. Jacobs
Committee Members,	Eric L. Petersen
	Adonios N. Karpetis
Head of Department,	Andreas A. Polycarpou

August 2018

Major Subject: Mechanical Engineering

ABSTRACT

The overall goal of this project is to improve upon existing engine control strategies used for large bore, lean-burn, natural gas engines in order to increase efficiency and maintain emissions compliance during variable fuel composition events. The objective of this work is to develop a full-scale engine simulation of a Cooper-Bessemer GMWH-10C that includes the actual kinematics of an articulated crank in addition to a set of solutions to calculate laminar flame speed for a range of alkane mixtures.

For engines with articulated cranks, the piston motion and port profiles are asymmetric and cannot be described as a simple slider-crank mechanism. The first part of this project was to derive the kinematic equations to explain this motion. The second part focused on the chemical kinetics and sought a way to generalize previously published equations to estimate laminar flame speed and ignition delay for a series of natural gas mixtures at a range of conditions. Then the developed piston motion, port profiles, and laminar flame speed equations were implemented into a full-scale engine model with predictive combustion capabilities that was tuned and validated against experimental data. In the future, this simulation can be used to develop control strategies to maintain performance and emissions compliance during variable fuel events.

DEDICATION

To Andre, my best friend

ACKNOWLEDGEMENTS

First and foremost, I’d like to thank my mother for being such a perfect example for strength and independence. She brought me into this world, and even though she often threatened to, never took me out of it.

If it weren’t for the encouragement and patience of Dr. Timothy Jacobs, I would not have entered into the graduate program – but I am so glad that I did. Over the past two years, he has provided so many opportunities that have helped me grow as an engineer and as a person, and I’m thankful for his confidence and faith in me.

A huge thank you to my peers in the Advanced Engine Research Lab who made going to campus everyday more fun. Especially Jake Hedrick who laid out the foundation of this project and helped me get started, and to Abdullah Bajwa who is great for bouncing ideas off of.

This project would not have been possible without the support of Pipeline Research Council International (PRCI), the expertise of Mark Patterson and Greg Beshouri, Gary Choquette, Dan Rem, Brad Jones, John Milliott, and Bob Goffin. Thank you all for your time and for sharing your knowledge.

Finally, I would like to thank the talented bands and composers who have gotten me through numerous early mornings and late nights all throughout my life. Music has been a source of inspiration and a study aid, an emotional release and a distraction, a way to remember and a way to forget. I will never meet these artistic strangers, yet their blessed voices, hands, and minds continue to inspire me.

Thank you!

CONTRIBUTORS AND FUNDING SOURCES

Contributors

This work was supervised by a thesis committee consisting of Professor Timothy Jacobs (advisor) and Professor Eric Petersen of the Department of Mechanical Engineering and Professor Adonios Karpetis of the Department of Aerospace Engineering.

This work improves upon codes and models previously developed by Jake Hedrick, a Masters student working under the supervision of Timothy Jacobs. All work conducted for the thesis was completed independently by the student.

Funding Sources

This work was made possible by the Pipeline Research Council International under contract number PR-457-14201-R04.

Its contents are solely the responsibility of the authors and do not necessarily represent the official views of the Pipeline Research Council International.

NOMENCLATURE

°bTDC	Degrees before top dead center
AERL	Advanced Engine Research Laboratory
BDC	Bottom dead center
C1	Methane
C2	Ethane
C3	Propane
C4	Butane
C5	Pentane
C5+	Pentane and heavier hydrocarbons
CAD	Crank angle degree
CFD	Computational fluid dynamics
CNG	Compressed natural gas
EIA	Energy Information Administration
EPC	Exhaust port close
EPO	Exhaust port open
FERC	Federal Energy Regulatory Commission
FMEP	Friction mean indicated pressure
HHC	Heavy hydrocarbons
HHV	Higher heating value
IC4	Isobutane
ID	Ignition delay
IMEP	Indicated mean effective pressure
IPC	Intake port close
IPO	Intake port open
LFS	Laminar flame speed
LH	Left hand

LHV	Lower heating value
LNG	Liquefied natural gas
MCC	Main combustion chamber
MN	Methane number
NC4	Normal butane
NGL	Natural gas liquids
PCC	Precombustion chamber
RH	Right hand
RMSE	Root mean square error
SI	Spark ignited/ignition
TDC	Top dead center
TER	Trapped equivalence ratio
SG	Specific gravity
WI	Wobbe index

TABLE OF CONTENTS

Page

LIST OF FIGURES

Page

LIST OF TABLES

1. INTRODUCTION

1.1 Executive Summary

The work presented in this paper seeks to understand the effects of natural gas variability on a lean burn, large bore, two-stroke integral compressor engine. This is part of a multi-phase project that seeks to develop engine control strategies to maintain prescribed engine operating conditions during variable fuel composition events in an effort to protect the equipment, maintain emissions compliance, and increase engine efficiency.

The types of engines under consideration for this project make up the majority of the engine fleet used in natural gas pipeline transportation, and most of these are over 50 years old. This has created the need to improve the engine controllers to adapt for changing operating conditions, namely the composition of the natural gas fuel.

Traditionally, natural gas consists of mostly methane with small amounts of ethane and even smaller amounts of higher hydrocarbons. However, increasing natural gas production from shale plays has led to significant composition fluctuations that directly impact the chemistry of the mixture. Most internal combustion engines, are designed to run on a narrow range of fuels. Operating outside of this range can have unintended consequences. Since the controllers on these engines do not currently account for fuel composition, the engine may have to be derated if it is running with a particularly hot fuel, sacrificing fuel efficiency and performance.

The attempted solution to this problem is to develop a full-scale simulation of a field engine in an industry-standard software in order to predictively study the in-cylinder combustion process. This may help further the understanding of combustion complexities and how it is related to overall engine operation. There is a significant investment to be made in developing a full-scale predictive combustion model in the amount of time, data collection, and computation required. However, once the model is developed and tuned, it becomes easier to conduct tests and analyze data.

When developing an engine model, knowledge of the engine geometry, such as piston profiles and port timings, is important to accurately model compression, expansion, and cylinder scavenging. The GMW engine has a V-configuration and an articulated crank. This means two power pistons are connected to one compressor master rod, and the power pistons are offset from the centerline of the crank. This leads to non-symmetrical motion about top dead center (TDC) for each piston. Additionally, each piston has a slightly different position profile depending on how it is connected to the compressor master rod. Because of this, a piston position profile modeling technique was developed based on engine geometry. It has been found that this can impact the intake port timing by about 10 CAD and the exhaust port timing by about 7 CAD from what would be expected by modeling the system as a slider-crank mechanism.

Also when developing an engine model, information about certain engine parameters, such as fueling, air manifold pressure, in-cylinder pressure, and emissions, etc. over a range of operating conditions is required to tune and validate the model. Therefore, a large set of data was tested onsite over the course of two days. This data was then evaluated and used to tune and validate the engine simulation.

The engine simulation software used is Gamma Technologies' GT-Power, a 0D/1D model solver that has become the industry standard for engine design and development. While this software is robust enough to determine overall engine performance for a given set of conditions, the chemical kinetic models contained in the software library are too simple to handle fuel mixtures. Therefore, in order to better model the fuel chemistry, it became necessary to develop a method of estimating certain fuel properties that relate directly to combustion and combustion phasing.

Chemical kinetics models can involve hundreds of species and thousands of reactions, making it impractical to evaluate these mechanisms in a real-time engine simulation. Therefore, the laminar flame speed (LFS) and ignition delay (ID) of natural gas mixtures were evaluated at a range of conditions using an open-source chemical kinetic solver, Cantera. This required modeling the reaction process in simple 0D and 1D reactors, like a mathematical model of a reaction vessel and shock tube. Once the data was collected from Cantera data, curve fits were developed using non-linear regression techniques. Only the LFS equation was implemented into the engine model. The ID equation is left for future implementation if necessary.

The major deliverable of this project was a predictive combustion model of the GMW engine designed in GT-Power. It includes actual engine geometry to represent the articulated crank motion in addition to an equation that can estimate LFS based off natural gas mixture. This full-scale engine model was successfully validated against experimental data to be within one sigma of indicated mean effective pressure (IMEP) and peak pressure for all relevant test conditions.

1.2 Motivation and Background

The vast majority of internal combustion engines are designed to run on a specific fuel blend for a particular purpose and are optimized for efficiency and emissions. As time progresses, the engine ages, the operating conditions may change, and emissions regulations become more stringent. Thankfully, technology improves as well. This allows for opportunities in which older engines and engine controllers can be retrofitted with new hardware or software. In some cases, this is a more cost effective option than a total engine upgrade or replacement.

Natural gas refers to a mixture of alkanes that is usually above 90% methane and may contain some amounts of ethane or other heavier hydrocarbons, sulfur, water vapor, nitrogen, and carbon dioxide. Conventionally produced natural gas from wellheads traditionally has a high methane content compared to natural gas from shale. Natural gas production from shale-based sources has increased substantially the past few decades and has been shown to vary geographically and temporally. [1] The Federal Energy Regulatory Commission (FERC) regulates the interstate pipelines, but it is usually left up to the pipeline operators to regulate the mixture composition. As more shale gas is introduced into the system, there is the possibility for the fuel quality to fluctuate more and eventually degrade over time. This directly affects the fuel’s chemical and combustion properties.

The engines at natural gas compressor stations power the compressors to transport the gas and are typically fueled by a sample of the mixture. Current engine controllers do not account for fuel composition, so operating conditions such as fueling amount and cylinder balancing are determined by a feedback loop in a reactive fashion. If the fuel composition changes too much, the engine performance, the efficiency, and the emissions may be negatively affected. Perhaps if engine performance could be predicted for a specific fuel composition, then engine controllers could be updated to allow for lower (or higher) quality gas to flow in the pipelines, similar to an automotive gasoline flex fuel engine that adjusts for high or low ethanol content. In this case, the controller would function more “actively” than “reactively.”

This study seeks to understand the impact of natural gas variability on a legacy pipeline engine by understanding how alkane mixtures affect certain combustion-relevant properties and integrating this information into a full-scale engine model for simulation.

1.2.1 History of Two Stroke Engines and Their Applications

Combustion engines are energy conversion devices: they convert the chemical energy contained within the fuel into a useable form via oxidation. There are different methods for inducting the air, adding the fuel, igniting the mixture, and exhausting the spent gases that give rise to the different types of internal combustion engines.

Arguably the most ubiquitous engine is the four-stroke cycle which is credited to Nicolaus Otto (1832 – 1891). However, Otto’s fame would not have been possible without the initial designs by Jean Joseph Etienne Lenoir (1822 – 1900) or the further development by Carl Eugen Langen (1833 – 1895). [2] This type of engine works by inducting and exhausting the gases in separate and distinct piston strokes. Once the implications of the four-stroke cycle’s success caught on, Dugald Clerk (1854 – 1913) simplified the mechanical design by combining the intake and exhaust strokes thus doubling the specific power. In doing so, he decreased the number of moving parts, effectively making the design more reliable. This has contributed to the continued use of two-stroke engines throughout the years despite certain downfalls when compared to their four-stroke counterparts.

Today, most of the largest and the smallest internal combustion engines are two-stroke. They are common in lightweight applications such as chainsaws and snow mobiles or in large applications such as for marine propulsion or power generation. The versatility in application is partially due to the fewer number of moving parts and higher power density.

1.2.2 The Spark Ignited Two-Stroke Cycle

Combustion begins when the piston is near top dead center (TDC). In a typical SI engine, the electrical arc discharge from the spark plug initiates the combustion process. This flame kernel begins a chain of exothermic reactions that grows and propagates through the mixture. The force from the expanding gases pushes the piston downward during the power stroke. As the piston moves down, first the exhaust port is uncovered (EPO) and the burned gases begin to flow out of the cylinder due to the pressure differential. Soon after, the intake port is uncovered (IPO) and fresh charge begins to enter the cylinder. At this time, both ports are uncovered and gases are both entering and leaving. The port placement and piston head shape is designed in such a way to direct the fresh charge up to the top of the cylinder so it doesn’t immediately short circuit and flow out of the cylinder. After the piston reaches bottom dead center (BDC), it begins to move upward. First the intake port is closed (IPC), then the exhaust port is closed (EPC). After EPC, the gases trapped within the cylinder are compressed until the piston reaches near TDC and combustion begins. From here, the cycle repeats.

1.2.3 Natural Gas Production and Transportation

Market economics have driven and directed the oil and gas industry starting from when Edwin Drake drilled the first commercial oil well in the U.S. in Titusville, Pennsylvania in 1859. The oil and gas industry is especially susceptible to price fluctuations due to the laws of supply and demand. This dictates where, when, and how big a well will be drilled, in addition to the selling price of the commodities.

Through the 1900s, conventional vertical wells were the norm because unconventional production methods were too expensive. George Mitchell, later called the father of the shale revolution, found a way to combine directional drilling and hydraulic fracturing and make it economically feasible around the 1990s. However, onshore natural gas production didn’t take off until after 2005 when two massive hurricanes reduced offshore production in the Gulf of Mexico by 15% and caused the price of oil and gas to skyrocket. This made shale wells more profitable, so more of them were constructed. Then, in 2008, an unanticipated financial crisis disrupted the economy, forcing crude oil prices down about 60% and natural gas prices down about 80%. This shifted the industry focus to NGL production, which soon caused NGL oversupply and prices dropped. Since then, crude oil prices have been slowly increasing while natural gas prices have stayed down. There are other important events that have impacted the oil and gas industry and caused its rises and falls, but these are perhaps the most important events with respect to natural gas production. [3]

This brief history of the oil and gas industry illustrates the volatility of the market and how prices and demand affect production and vice versa. Thanks to George Mitchell, shale gas production is steadily increasing every year. While wellhead natural gas composition has not been found to fluctuate significantly within a country, it does significantly change on a global scale. Furthermore, the increased production of shale gas has broadened the raw compositions, so as to increase the amounts of higher hydrocarbons produced even within a small geographic region. [1]

According to the U.S. Energy Information Administration (EIA), an average of 73.6 billion cubic feet per day (Bcf/d) of natural gas was produced in 2017. Amazingly, this is the first time since 1957 that the U.S. exports have exceeded the imports, mainly due to the high levels of production from the many shale plays across the country. [4] Of total production that year, about 16.8 trillion cubic feet were produced from shale, equaling about 60% of total dry, or consumer-grade, natural gas production. In fact, shale natural gas production has grown so much that pipelines that historically flowed from the Gulf of Mexico to the Northeast are reversing and flowing the other way. Natural gas production is projected to increase drastically over the next few decades, with gas coming from shale-based sources making up the biggest percentage.

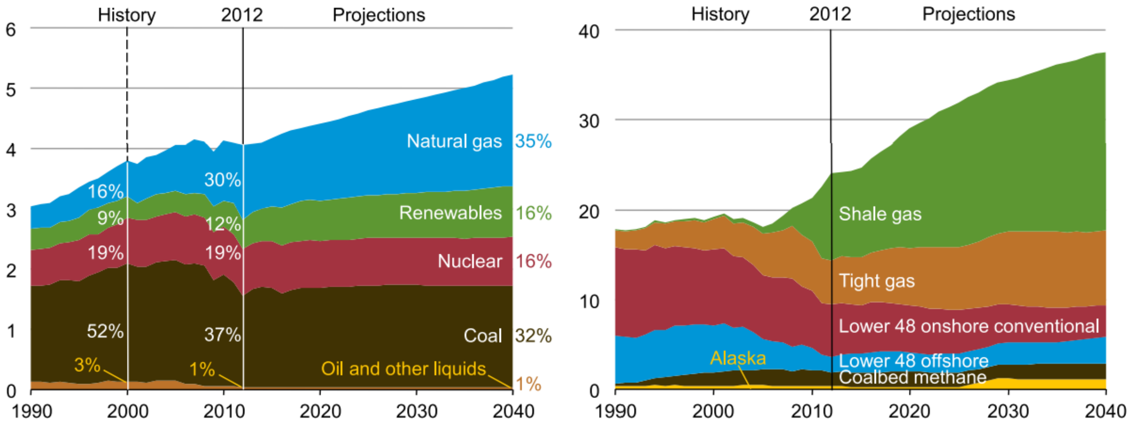

Figure 1: (Left) Past and projected electricity generation in trillion kilowatt-hours. (Right) Past and projected sources of U.S. production of natural gas in trillion cubic feet. Reprinted from [4]

A map of U.S. shale plays is shown in Figure 2. Currently, the most active shale plays in the U.S. are the Barnett, Haynesville, and Eagle Ford plays in the South and the Marcellus and Antrium in the Northeast. [5] Figure 3 shows the natural gas pipelines and compressor stations in the U.S.

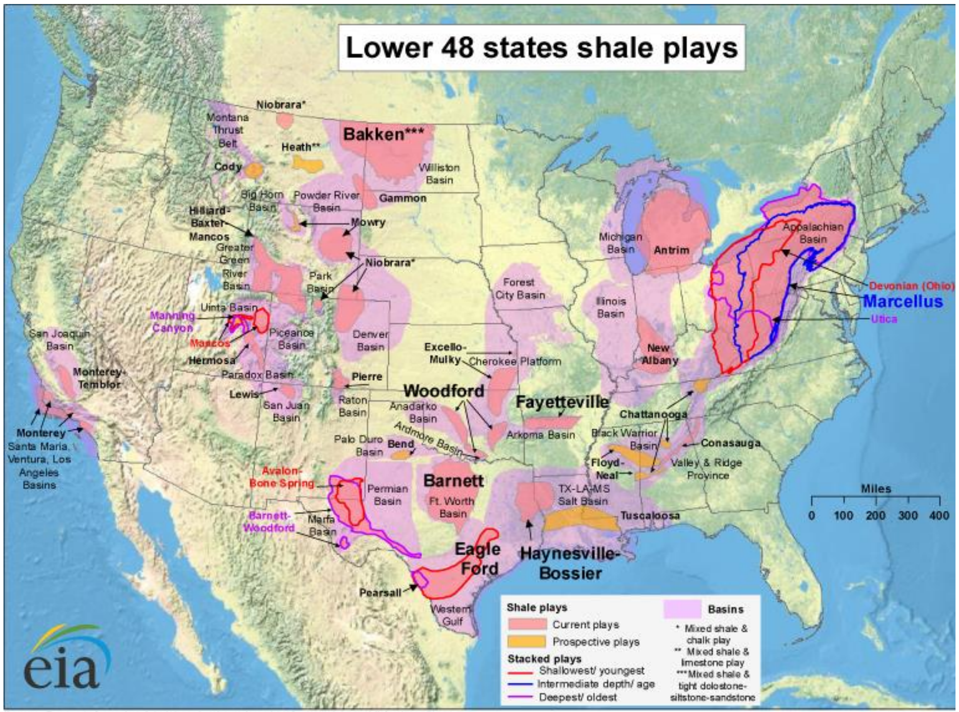

Source: Energy Information Administration based on data from various published studies.
Updated: May 9, 2011

Figure 2: Shale plays in the US as of May 2011. Reprinted from [6]

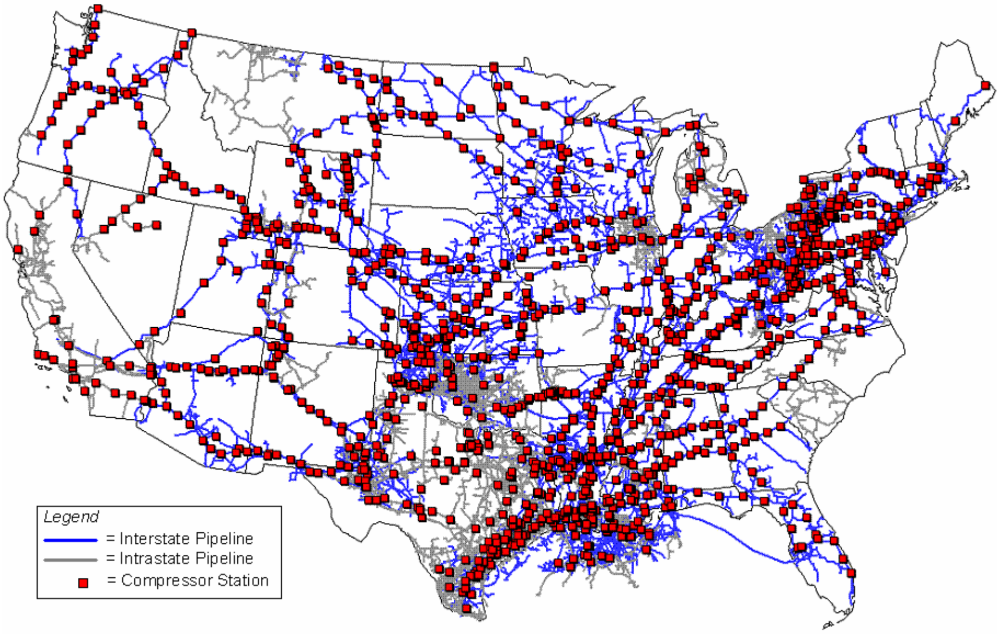

Figure 3: U.S. Natural Gas Pipeline Compressor Stations. Reprinted from [7]

There are over 305,000 miles of transmission pipelines and more than 1,400 compressor stations in the U.S. located between 50 to 150 miles apart. [8] They operate continuously to pressurize the gas and overcome the inherent frictional pressure losses and filter the gas to remove water, condensates, or sand. The flow rate of gas through the station depends on the upstream and downstream conditions. In other words, the load of the engines and the compressor depends on the needs of the overall pipeline system.

In 1938, the Natural Gas Act was passed in order to cap the rates of natural gas and to form the Federal Power Commission (which later formed into FERC). It was the first piece of federal legislation involving natural gas regulation, but it excluded production and gathering. Since then, the Natural Gas Act of 1938 has had multiple amendments, other laws have been passed, and the price cap has been removed. [9] Today, there are multiple federal agencies that regulate and manage the usage of pipelines including FERC and the U.S. Department of Transportation (DOT) in addition to state agencies that regulate intrastate lines. FERC oversees the operation and construction of interstate pipelines, storage, and the composition of gas allowed to be put into the pipeline. The definition of pipeline quality gas varies from pipeline to pipeline, and there is currently debate of standardizing the quality regulations.

The processing requirements to make shale gas marketable depend on the initial composition. It is better to process the gas as little as possible to keep costs low while still maintaining a level of interchangeability or fungibility. Interchangeability means the ability to substitute one mixture for another without negatively affecting safety, performance, or pollutant formation. This is important because it allows for one company to put gas into one side of the pipeline and sell it on the other end without waiting for the actual gas molecules to traverse the length of the line. On the natural gas market, sales and transactions are usually conducted on a heating value basis, so there is increasing concern for the composition of the gas and its other properties. [9]

In 2005, a council called NGC+ Interchangeability Work Group submitted a white paper to FERC with four recommendations on regulating pipeline quality. They are as follows: Wobbe index (WI) for a given area should not exceed +/- 4% of the local historical average (maximum of 1,400 BTU/scf), heating value should not exceed 1,100 BTU/scf, butanes and heavier hydrocarbons should not exceed 1.5 mol%, and total inerts (CO_2, N_2, etc.) should not exceed 4 mol%. [10] FERC considered these guidelines, but instead of setting strict limits, established five gas quality policy principles:

1. Only the specifications contained in a FERC-approved gas tariff can be enforced.
2. Pipeline tariff provisions must be flexible for future changes and safety.
3. Pipeline operators and their customers should develop gas quality and interchangeability specifications based on “sound technical, engineering and scientific considerations.”
4. In developing the specifications, it is encouraged to use the NGC+ guidelines as a reference.
5. If the pipeline operators and customers cannot agree, then FERC will review the issue on a case-by-case basis. [11] [12]

There can also be higher amounts of heavy hydrocarbons (HHCs) in the pipeline due to rejection. If the price of a pure species drops too low, it is can be more profitable to keep it in the natural gas mixture and sell it at natural gas prices. An example seen today is the overproduction of ethane. Liquid ethane is used to make ethylene in olefin crackers that is then used to make plastic products and other commodities. If there is a surplus of ethane, the market price may drop to be below the price of natural gas. In which case, it is no longer profitable to separate out all the ethane. This has led to ethane rejection, which is the process of rejecting excess ethane to the pipeline and selling it as natural gas at natural gas prices. [3] Propane is typically the second largest component of NGL, but it is not produced in high enough quantities to warrant rejection.

While monitoring the higher heating value (HHV) can protect the buyer and seller, the heating value may not be particularly useful for engine control. As of 2005, there were approximately 5,600 engines on natural gas pipelines in the U.S. generating over 9.1 million bhp. [13] Approximately 70% of these are lean burning, two-stroke, turbocharged engines manufactured over 50 years ago and, due to their reliability, will likely be in operation for many years to come. Since these engines make up the vast majority of the fleet, there is interest in increasing their efficiency and decreasing pollutant production, especially during a variable natural gas composition event.

The specific model for consideration is a Cooper-Bessemer GMWH-10C. These were produced from around 1946 to 1965 for the specific task of running compressors for natural gas pipeline transportation. They are no longer in production, but there are around 600 engines from the Cooper-Bessemer GMW family still in operation. [14] For this reason, it is important to maximize the efficiency of these engines because the fuel consumption has a large financial impact to the owners and operators.

1.3 Objective

The objective of this work is to develop a full-scale engine simulation of a Cooper-Bessemer GMWH-10C that includes the actual engine geometry and a predictive combustion model that can be used to develop control strategies to maintain performance and emissions compliance during variable fuel events.

2. LITERATURE REVIEW

2.1 Cooper-Bessemer Research

Some Cooper-Bessemer engines date back to the 1940s. By today’s standards, these original models had poor efficiency and high emissions. Many of these engines have been retrofitted with electronic fuel injectors, exhaust after-treatment systems, and more sophisticated engine controllers to combat the ever increasing emissions regulations. It is usually more cost effective to apply hardware and software updates to these engines than it would be to suffer the high cost of a total upgrade. [14] In some laboratories and universities, these engines are still being studied to better understand the fundamental operation and to test new technologies.

Several studies at Colorado State University’s Engines & Energy Conversion Lab have illustrated differences between the piston banks of a Cooper-Bessemer GMV-4TF. In one particular study, the airflow characteristics were quantified and simulated. It was found that the amount of trapped mass between the cylinders were different and that some cylinders consistency had higher maximum temperatures which directly affects NOx production. [15] Later, another study was done to successfully develop cylinder-level fuel and ignition control techniques with the specific goal of decreasing NOx. Two strategies were developed: one which maintained NOx while decreasing fuel consumption and the other which maintained fuel consumption but reduced NOx emissions. [16]

There have also been numerous tests to evaluate scavenging efficiency and trapped air/fuel ratio in the GMV-4TF using the tracer gas method. From this, equations to evaluate trapping efficiency, scavenging efficiency, and trapped air/fuel ratio were developed. [17] From this, nitrous oxide was used as the tracer gas to further study the effects of various engine operating conditions such as boost pressure, speed, back pressure, and intake port restriction on scavenging efficiency and trapped air/fuel ratio. [18]

Prechambers are small cylindrical volumes (typically about 1 – 2% of the cylinder clearance volume) that are attached to the main chamber. These devices are commonly used to reduce NOx emissions by extending the lean burn limit and reducing combustion variability. When the in-cylinder mixture is too lean, CO and HC emissions increase due to misfire and combustion instabilities, so a prechamber is used to promote initial flame kernel growth in a locally stoichiometric fuel and air mixture. This creates a partially burned mixture that is then jetted into the main chamber to continue the combustion process. Prechambers in the Colorado State University’s GMV have been experimentally tested in order to study the heat release, pressure profile, and jet velocity and how these increase with increasing prechamber equivalence ratio. [19] Other studies include nozzle designs [20], synthetic gaseous (syngas) fueling [21], and extensive computational fluid dynamic (CFD) modeling [22]. There has not been such detailed studies conducted on the engine of interest for this report, so this previous work is used for reference.

Additional work on articulated cranks has involved studying secondary piston motion such as axial, lateral, and rotational variations that result from geometric clearances. In one such study, equations to calculate secondary motion of the piston crown, skirt, wristpin, and connection rod of an articulated piston were derived and then compared with the motion of a conventional system. [23] In addition to this, other detailed work has been done on developing robust simulations of Cooper-Bessemer engines. In one such case, a Cooper-Bessemer GMVH-12 model was successfully developed in SciLab. [24]

2.2 Natural Gas

Natural gas is odorless, colorless, and tasteless. It is used in a variety of applications, but the name does not refer to a specific chemical mixture. Rather, it refers to a mixture – any mixture, really – of alkanes that is at least 90% methane or as low as 85% in some cases. The remaining percentage can be alkanes including ethane, propane, normal butane, isobutane, and pentane, in addition to inerts such as nitrogen and carbon dioxide. There can also be a small percentage of sulfur and water vapor.

Natural gas stored as a compressed gas is called compressed natural gas (CNG). CNG is typically used in vehicles as a fuel. Liquefied natural gas (LNG) is cooled and condensed methane (-162°C or -260 °F at 1 atm). Natural gas is usually turned into LNG for transportation because it does not require a highly pressurized vessel. Due to the volume reduction from gas to liquid, the energy density of LNG is about 2.5 times greater than that of CNG at 250 bar. This should not be confused with natural gas liquids (NGLs), sometimes called condensates, which are ethane, propane, normal butane, isobutane, and pentane. NGLs are more valuable as a species than as a fuel, and they must be processed and separated. Liquefied petroleum gas (LPG) consists of propane, normal butane, and isobutane because these species liquefy at relatively low pressures. It is commonly used for cooking.

Sometimes a component of natural gas (specifically the NGLs) are more valuable as pure species. Most of these species can be used as a petrochemical feedstock, but they also have their individual market niches. Propane is mostly used for heating or cooking, normal butane is used as an additive in gasoline, and isobutane is used to increase the octane rating of premium gasoline.

2.2.1 Natural Gas Composition

2.2.1.1 Wellhead Gas

When extracting gas out of a conventional reservoir, the decrease in pressure is the common cause of gas composition change because it affects the chemical equilibrium. One of the first attempts to quantify natural gas compositions and bulk gas properties of wellhead gas reviewed the Wobbe Index (WI) of fuels from 26 cities around the U.S. It was found that the WI ranged from 1331 to 1357 BTU/scf, with a maximum of 1418 BTU/scf and minimum of 1201 BTU/scf. It was concluded that some areas showed stable fuels while others had continuous fluctuations within a specific range. [25]

Another study considered how composition variation would affect natural gas vehicles, so the time history of the WI for fuels at different locations within a 200 mile radius were studied. It was found that the statistics were similar to the national study [25] indicating that the statistics for this study could be applied nationally. [26]

Additional studies have been conducted on a global scale and have found broader compositional changes in some geographic regions and even some locations where the composition varies seasonally. [27] [28] [29] [30] This report focuses on fuel composition within the U.S. so global reports will not be discussed at length.

2.2.1.2 Shale Gas

Shale gas is typically considered “unconventional” because it is not the traditional method of natural gas production. The formation of natural gas in a shale play is dependent on the amount of organic matter, the type and permeability of the rock, the adsorption and diffusion rates, and other macro-scale and micro-scale interactions. [31]

Some modeling has been done to understand and predict gas composition based on the interaction of chemical and physical parameters. One such work created a numerical model based upon multicomponent Langmuir desorption to predict gas composition change during production by estimating diffusion and desorption of the gas through fractures in the rock assuming Darcy permeability and laminar flow. This is a complex process and had mixed results, partially because an accurate way to characterize permeability has not been established and flow inside fractures may be non-Darcy or turbulent. [32] In other attempted efforts, a more complex model was developed that used non-Darcy flow to estimate slip flow, transition flow, and free molecular flow with good results. [33] Overall, permeability, hydraulic fracture length, and flow rate changes caused by production interruptions have been shown to have strong influences on gas composition.

While there is still much work to be done to properly model the formation and accumulation of shale gas, for now, engineers and technicians will have to work with analyzing the compositions and trends after the gas has been extracted. This is much easier to measure and analyze, and there are large amounts of data already available based on production location.

In one survey, the composition from randomly selected wells in the Barnett, Marcellus, Fayetteville, New Albany, Antrium, and Haynesville plays were compared. The data was normalized to the reported compounds, and most compositions fell within the range of 85 to 95% methane, 0 to 3% carbon dioxide, and 0 to 1% nitrogen with the remaining amount some mix of ethane and propane. Of notable interest is the Antrium shale gas which ranges from a mixture partially made of 27.5% methane and 65% nitrogen to a mixture partially made of 85.6% methane to 0.7% nitrogen. The Marcellus and Barnett shale gas typically had the highest amounts of ethane ranging as high as 16.1 and 11.8%, respectively, whereas the other locations were between 1 and 3%. [5]

With respect to pipeline compositions, one report looked at the effect of adding gas from the Marcellus play into a pipeline. Before the addition of the shale gas, the pipeline had a stable heating value of around 1040 BTU/scf. Afterward, there were fluctuations between 980 to 1350 BTU/scf with an average of 1155 BTU/scf and ethane levels between 1 to 16%. [34]

In another survey conducted in 2014, 6,330 samples from interstate pipelines were statistically analyzed. It was found that the HHV ranged between 749 and 2567 BTU/scf with an average of 1041 BTU/scf. This large range is caused by the range of values reported in carbon dioxide, nitrogen, ethane, butane and higher hydrocarbons, and hydrogen. [35] This shows the extreme ranges seen in pipelines all across the U.S. The statistics are summarized in Table 1.

Table 1: Statistics on gas composition in interstate transportation pipelines. Reprinted from [35]

	HHV (BTU/scf)	LHV (BTU/scf)	SG	CO_2%	N_2%	C_2%	C_4+%	H_2
Max	2567	2362	1.522	50.00	16.81	100.0	17.97	30.00
Min	749	675	0.409	0.00	0.00	0.00	0.00	0.00
Avg	1041	939	0.598	0.56	1.73	5.07	0.14	0.01

An example of a heating value fluctuation that occurred at an undisclosed location over the course of a few days is shown in Figure 4.

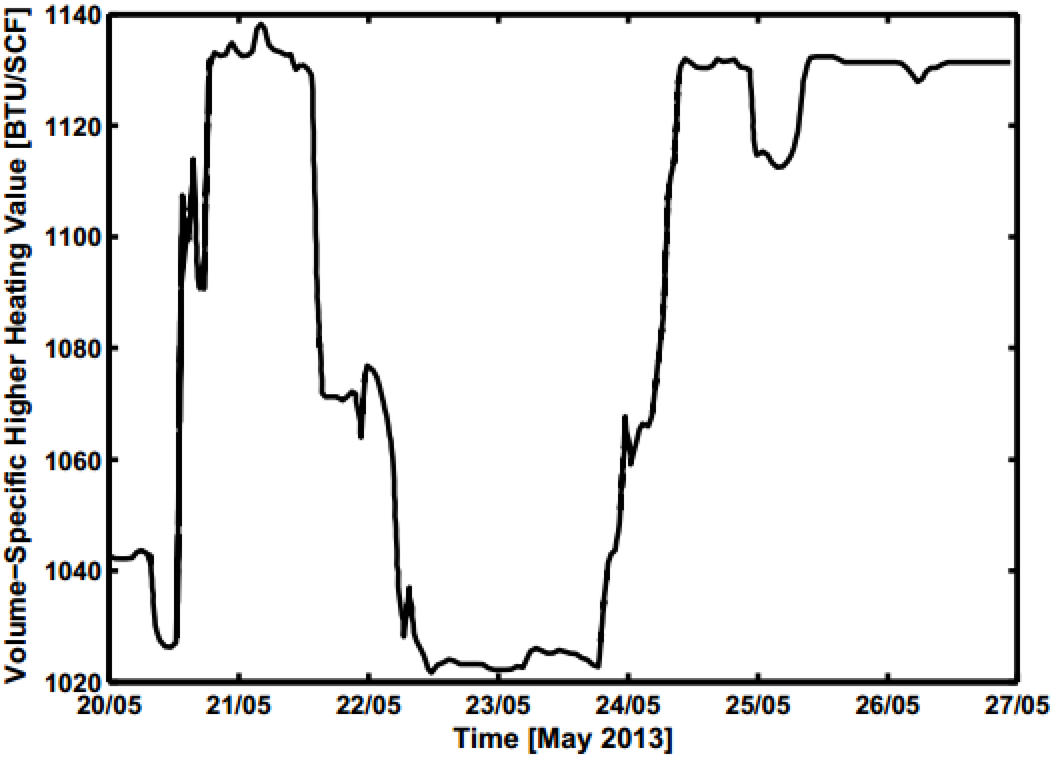

Figure 4: Higher heating value fluctuation over the course of a few hours at an undisclosed location. Reprinted from [35]

Thus it can be concluded that natural gas from shale reservoirs exists in a larger range of compositions than has previously been seen in wellhead gas. The composition fluctuation is also greater due to chemistry and physics based phenomena. Since the pipeline gas changes temporally and geographically, the shifts can be sudden and last anywhere from hours to days to months. This is the challenge that current natural gas pipeline and compressor station operators face.

2.3 Combustion

When modeling combustion in an engine, laminar flame speed (LFS) and ignition delay (ID) are required to determine the combustion phasing and thus the rate of heat release. The cylinder pressure can be determined from the thermodynamic relationship to the heat release rates using a two-zone combustion model that uses the laminar flame speed to determine the rate of mass burned. This is described further in Section 2.4.

The LFS and ID can be calculated using chemical kinetics models that have been validated against experimental data collected at a range of temperatures and pressures.

2.3.1 Laminar Flame Speed

Laminar flame speed is defined as the velocity of a laminar fuel and air mixture moving into a flame front relative to the flame. It is a property of the fuel and air mixture. More specifically, it is dependent on the temperature and species concentrations in the flame and the transport and thermodynamic properties of the mixture.

Experimentally, LFS is measured by using a closed spherical vessels to contain a homogenous, quiescent mixture and then placing a spark in the middle to propagate a flame outward. While there are complications to test high initial temperatures and pressures, this is currently the most accurate method to estimate laminar flame speed for SI engines. [2] Other measurement techniques include using a Bunsen-burner or a flat-flame burner. [36] For a given fuel at a set of initial conditions, the LFS decreases as the equivalence ratio decreases, but the LFS peaks slightly rich, usually around 1.1 or 1.2. Other general trends that increase LFS are as follows: increasing temperature, decreasing pressure, decreasing residual fraction. [37]

Arguably the most commonly used LFS correlation was developed by Metghalchi and Keck. In this experiment, a series of mixtures at engine-relevant conditions were tested and the measured LFS were correlated to a simple power law.

$$S_L = S_{L0} \left(\frac{T_u}{T_0}\right)^{\alpha} \left(\frac{P}{P_0}\right)^{\beta} \tag{1}$$

where S_{L0}, α, and β are fitted constants. The coefficients were fit for specific mixtures. Later, it was found that the temperature and pressure exponential were functions of equivalence ratio and independent of fuel type. S_{L0} was found to be a weak function of fuel type, and instead was broken into parameters: B_2 which is a fitted value, and B_m and ϕ_m which are the flame speed and equivalence ratio at the maximum flame speed for the specified fuel mixture. [38]

$$S_L = [B_m + B_2(\phi - \phi_m)] \left(\frac{T_u}{T_0}\right)^{2.18-0.8(\phi-1)} \left(\frac{P}{P_0}\right)^{-0.16+0.22(\phi-1)} \tag{2}$$

There have been multiple attempts at fitting this equation at a range of temperatures, pressures, and equivalence ratios, but these results are only for specific fuel mixtures and result in different coefficients. [39] [40] There has not been much work conducted to generalize the equation for a range of fuel compositions.

Metghalchi and Keck's equation has been implemented into GT-Power with the following form. It includes a term to account for the dilution effects. [41]

$$S_L^o = \left(B_m + B_\phi(\phi - \phi_m)^2\right) \left(\frac{T}{T_{ref}}\right)^\alpha \left(\frac{P}{P_{ref}}\right)^\beta (Dilution) \tag{3}$$

where

$$Dilution = 1 - 0.75D(1 - (1 - 0.75 * D * X_{res})^7) \tag{4}$$

Turbulent flame speeds, on the other hand, are dependent on the shape of the flame and the in-cylinder gas motion. They are dependent on the mixture properties in addition to the motion of the flow. Typically, they can be as high as 10 times the LFS due to the wrinkling and stretching effects on the flame front that increase the surface area. [2] Turbulent flame speeds are important to the combustion process, but they will not be covered in depth in this project. Instead, they will be accounted for via a turbulent flame speed multiplier in the flame speed model.

2.3.2 Ignition Delay

In the world of combustion science, ignition delay (sometimes called the induction time) refers to the length of time it takes for a homogeneous fuel and air mixture to combust. This is usually measured using a shock tube or rapid compression machine

In the world of engines, ignition delay can have several different meanings depending on the context. In compression ignition engines, ignition delay refers to the time between start of injection and the start of combustion. In SI engines, burning starts immediately after the spark ignites. Therefore, for an SI engine, ignition delay refers to the time between the spark to when a small but significant amount of mass has burned, usually 1% or 2%. This happens concurrently with noticeable in-cylinder pressure rise and is used as a reference point to indicate when the flame front has been developed and energy release has begun. [42]

Engine ignition delay should not be confused with knocking, or end-gas autoignition, which is when some amount of fuel-air mixture combusts outside of the flame front. This happens when the flame front does not reach some of the fuel and air mixture before the temperature and pressure rise high enough to cause the unburned mixture to autoignite. This can cause severe pressure spikes that negatively impact engine performance and may lead to structural damage. In the large bore, SI engine being studied in this project, knocking is typically not an issue.

The popular equation developed by Livengood and Wu predicts autoignition to occur when

$$1 = \int \frac{1}{\tau(\theta)} d\theta \qquad (5)$$

where θ is the crank angle degrees and τ is the ignition delay. [43]

For this report, the form of the equation to estimate the ignition delay time was developed by Douaud and Eyzat. [44]

$$\tau = \beta_1 \left(\frac{MN}{100}\right)^{\beta_2} P^{\beta_3} \exp(\frac{\beta_4}{T}) \qquad (6)$$

After there was only moderate success with this form, it was found that the methane number (MN) may not be a good octane number surrogate due to the differences in experimental testing method. MN is a measure of the fuel's propensity to knock. The MN correlation used for this project was developed by Choquette and has been shown to have reasonable results when compared to experimental data and other correlations. [35]

Therefore, Hedrick reevaluated the equation and added terms to relate the equivalence ratio and residual fraction to the ignition delay time. [45]

$$\tau = \beta_1 \left(\left(\frac{1}{\phi}\right)^{\beta_5} \frac{MN}{100} (1 - \beta_6 X_{res})\right)^{\beta_2} P^{\beta_3} \exp(\frac{\beta_4}{T}) \qquad (7)$$

This form of the equation was used to fit the ignition delay data for this report. After fitting the correlation, the fit was not implemented into GT-Power due to the limitations of 0D and 1D modeling in the software.

2.3.3 Cantera Software

Cantera is an open-source software package for solving chemically reacting flows. It can be used to evaluate both thermodynamic and transport properties, homogenous and heterogeneous kinetic rates, chemical kinetics and equilibrium, among other items that may be of interest in a reaction. [46] Cantera's toolkit is written in C++, so a Python interface was used to simplify the coding. This Python code was originally developed by Jacob Hedrick under Dr. Timothy Jacobs. [45] In this project, it was developed further to allow for larger chemical mechanisms and mixtures.

The code works by first taking the user-defined fuel species mole fractions, the equivalence ratio, initial pressure, initial temperature, and residual gas fraction and converts it into molar concentrations for the LFS and ID solvers. The residual gas composition is determined from stoichiometric combustion products. Once the mixture has been initialized, it is either passed to a 1D free flame object for LFS calculation or to the 0D homogenous constant volume ideal gas reactor object to calculate ID.

The LFS is determined by first initializing the gas mixture object as described previously. Then, a free flame object is initialized with an initial grid, steady-state and absolute tolerances, and an initial time step. Every 20 iterations, the Jacobians are evaluated. When this is done, the numerical solver reduces the time step until the grid points converge. Next the inlet mass flux for the first order estimated flame speed is guessed. Solutions are attempted first with heat transfer disabled, meaning assuming an adiabatic flame with an imposed temperature rise over the flame thickness to estimate intermediate species, second with heat transfer and grid refinement enabled, third with multicomponent diffusion. The resulting LFS is the speed of the flow into the free flame at the first node. [45]

The ID is determined using a 0D homogenous constant pressure ideal gas reactor using time steps at the prescribed initial temperature and pressure. ID can be defined in several ways: peak of OH formation, start of CH* formation, initial pressure rise, or maximum temperature rise. For this project, OH formation is used. First the object is initialized with the gas mixture and the reactor walls as adiabatic. A default time step of 1e-7 s was used to resolve all the fast intermediate species. The time steps continue until a temperature change of 50 K is detected, then the simulation is ran for another 5e-4 s. Once this is completed, the temperature inflection and the OH inflection is determined. If the OH curve does not have an inflection, then combustion is assumed to not occur. The ID is calculated by a linear fit on the OH curve until the detected temperature rise. [45]

2.4 GT-Power Engine Modeling

GT-Power, created by Gamma Technologies, is a 0D/1D model solver that has become the industry standard for engine design and development. It is a robust software that can be used to model spark ignition, compression ignition, homogenous charge compression ignition, and multi-fuel combustion for either steady-state or transient analysis. Thermal, acoustic, emissions, and combustion models are included in the software library. Most of these are basic, rudimentary models published and examined in literature. Thankfully, GT-Power users have the capability to write and add their own models or programs. Because of these reasons, and due to its prevalence and acceptance in the industry, this program was selected for use on this project.

2.4.1 Predictive vs. Non-Predictive Combustion Models

Combustion modeling can be split into three groups: non-predictive, predictive, and semi-predictive. Non-predictive models use a prescribed burn rate as a function of crank angle to calculate the combustion phasing regardless of in-cylinder conditions as long as there is enough fuel to support the total mass burned. The most common type of a non-predictive model uses a Wiebe function. Predictive models calculate the burn rate from the in-cylinder pressure, temperature, residual fraction, and equivalence ratio. Typically, non-predictive models run faster but there is a potential loss of accuracy depending on the independent variables being tested. For example, a non-predictive model would be good to use to test a variable that doesn't directly affect combustion such as intake manifold volume, but it would not be good to test the effects of fuel injection timing or duration. In addition to the two major categories, there are also semi-predictive combustion models. This type uses non-predictive models but can change certain coefficients based on significant input variables. For example, a Wiebe function can still be used, but the Wiebe parameters would be calculated based on the input variables. [41]

In the developed GT-Power model, a two-zone predictive spark-ignition turbulent flame model is used. This model was designed for homogenous charge, SI engines. It calculates the burn rate from cylinder geometry, spark location, spark timing, air motion, and fuel properties. The mass entrainment rate and the burn rate are determined from the following three equations

$$\frac{dM_e}{dt} = \rho_u A_e (S_T + S_L) \tag{8}$$

$$\frac{dM_b}{dt} = \frac{M_e - M_b}{\tau} \tag{9}$$

$$\tau = \frac{\lambda}{S_L} \tag{10}$$

where M_e is the unburned mixture entrained mass, t is time, ρ_u is the unburned mixture density, A_e is the entrainment surface area at the flame front, S_T is the turbulent flame speed, S_L is the laminar flame speed, M_b is the burned mass, τ is the time constant, and λ is the Taylor microscale length. From this set of equations, it is easy to see that the time constant is equal to the ratio of Taylor microscale length to the laminar flame speed. The mass burned rate is equal to the difference between the entrained mass and the burned mass divided by the time constant. The rate of mass entrainment is proportional to the unburned gas density, the flame front area, and the sum of the laminar and turbulent flame speeds. [41]

In a two-zone combustion model, all cylinder contents are placed into the unburned zone, and a burned zone is initialized. For each time step, an amount of mass moves from the unburned zone into the burned zone. This is defined as the burn rate and is either prescribed for a non-predictive model or calculated for a predictive model. After every small amount of mass is transferred into the burned zone, the chemical equilibrium of the whole burn zone is calculated. This is done by assuming 11 products of combustion: N_2, O_2, H_2O, CO_2, CO, H_2, N, O, H, NO, and OH. After determining the new composition of the burned zone, the internal energy of the burned zone is calculated by summing the internal energy of each species. Finally, the new burned zone temperature and pressure are calculated. In essence, these steps are fulfilled via the following two equations.

$$\frac{d(m_u e_u)}{dt} = -p\frac{dV_u}{dt} - Q_u + \left(\frac{dm_f}{dt}h_f + \frac{dm_a}{dt}h_a\right) + \frac{dm_{f,i}}{dt}h_{f,i} \qquad (11)$$

$$\frac{d(m_b e_b)}{dt} = -p\frac{dV_b}{dt} - Q_b - \left(\frac{dm_f}{dt}h_f + \frac{dm_a}{dt}h_a\right) \qquad (12)$$

Where m is the zone mass, e is the zone energy, p is the cylinder pressure, V is the zone volume, Q is the zone heat transfer rate, and h is the enthalpy. The subscript u refers to the unburned zone, b refers to the burned zone, a refers to air, f refers to fuel, and f, i refers to the injected fuel. The terms in the above equations encompass the pressure work, heat transfer, combustion energy, and for the unburned equation, enthalpy addition from fuel injection.

2.4.2 *Woschni Heat Transfer*

In typical engine operation, a significant portion of energy leaves the cylinder as heat transfer to the walls. One of the most popular heat transfer model was developed by Woschni in 1967. [47] There have been multiple coefficients proposed for the equation, but the one used in this project is referred to as WoschniGT in GT-Power. [41] The coefficients for this model are lower during the gas exchange process when compared to the classical Woschni model thereby decreasing the total heat transfer. It has been recommended to use this form when there is no swirl data available.

$$h_c = 3.014B^{-0.2}p^{0.8}T^{-0.5}w^{0.8} \tag{13}$$

Where h_c is the in-cylinder heat transfer coefficient, B is the cylinder bore, p is the instantaneous cylinder pressure, T is the instantaneous cylinder temperature, and w is the average cylinder gas velocity. The average cylinder gas velocity is calculated from

$$w = C_1\overline{S_p} + \frac{C_2V_dT_r}{p_rV_r}(p - p_m) \tag{14}$$

where C_1 and C_2 are constants defined at different parts of the cycle, $\overline{S_p}$ is the average piston speed, V_d is the displacement volume, T_r is the mixture temperature, p_r is the mixture pressure, V_r is the mixture volume, p is the instantaneous in-cylinder pressure, and p_m is the motored in-cylinder pressure at the same crank angle as p. For this particular Woschni model, C_1 is defined as

$$C_1 = 2.28 + 3.9MIN(\frac{\dot{m}_{in}}{m_{cyl} * rpm}, 1) \tag{15}$$

Where $\dot{m}_{in}$ in the instantaneous mass flow rate, m_{cyl} is the instantaneous cylinder mass, rpm is the engine rpm. C_2 is zero during cylinder gas exchange and compression and 3.24e-3 during combustion and expansion.

An important part of calculating heat transfer is a proper estimate of the cylinder wall temperatures. The suggested values to use for full load are 550 – 600 K for the cylinder head and piston, and 400 K for the walls. [41] Due to lack of experimental data, these values were used as imposed boundary conditions with 550 K as the cylinder head and piston temperature. However, these values could be higher or lower depending on the actual operating condition.

2.4.3 In-Cylinder Flow

When modeling combustion predictively, the in-cylinder swirl, tumble, and turbulence are important influences on the flow velocity and turbulent intensity, so it is equally important to model the in-cylinder flow predictively. The velocity is used in the heat transfer model, and the turbulence values are used in the predictive combustion model and the heat transfer model. [41]

The in-cylinder flow model divides the cylinder into the central core region, the squish region, the head recess region, and the piston cup region. In each region at every time step, the average radial, axial, and swirl velocities are calculated. The cylinder chamber geometry, the piston motion, and the flow rates of the entering and exiting gases are used to calculate the instantaneous average turbulence intensity and turbulence length scale. The turbulence model working by solving differential equations for angular momentum, turbulent kinetic energy, and turbulent dissipation in three regions: the squish area near the piston crown, the cup volume, and the area near the cup lip.

When modeling in-cylinder gas flow predictively, the swirl and tumble motion of the incoming fluid is important. The swirl and tumble coefficients must be prescribed to calculate the torque applied to the in-cylinder gases. These coefficients are defined as the ratio of angular momentum flux to the linear momentum flux and can be calculated from torque measurements.

$$C_s = \frac{2T}{\dot{m}U_{is}B} \tag{16}$$

$$C_t = \frac{2T}{\dot{m}U_{is}B} \tag{17}$$

$$U_{is} = \sqrt{RT_o}\left(\frac{2\gamma}{\gamma-1}\left(1 - P_R^{\frac{\gamma-1}{\gamma}}\right)\right)^{\frac{1}{2}} \tag{18}$$

where C_s and C_t are the swirl and tumble coefficients, T is the torque,$\dot{m}$ is the mass flow rate, U_{is} is the isentropic valve velocity, B is the cylinder bore, P_R is the absolute pressure ratio, R is the gas constant, T_o is the upstream stagnation temperature, and γ is the specific heat ratio. The swirl and tumble coefficients can be positive or negative, and the sum of their absolute values must be less than or equal to unity to satisfy momentum conservation. [41]

2.4.4 Scavenging

The scavenging process in two-stroke engines is rather complex. One of the first detailed studies was done in 1914, and the concepts of perfect displacement and perfect mixing were developed. [48] In the perfect displacement model, the incoming fresh charge remains undiluted and simply displaces the spent gases. In the perfect mixing model, the incoming charge mixes with the exhaust gases and this mixture is what leaves the cylinder. These two proposed ideas are perfect idealizations; real scavenging is somewhere in-between and also includes some short-circuiting. [49]

The cylinder residual ratio is the instantaneous ratio of mass of burned gases to the total mass of gases within the cylinder. The exhaust residual ratio is the instantaneous ratio of mass of burned gas to the total mass of gases leaving the cylinder. The scavenging ratio is the ratio of mass of trapped air to the total trapped mass. [2]

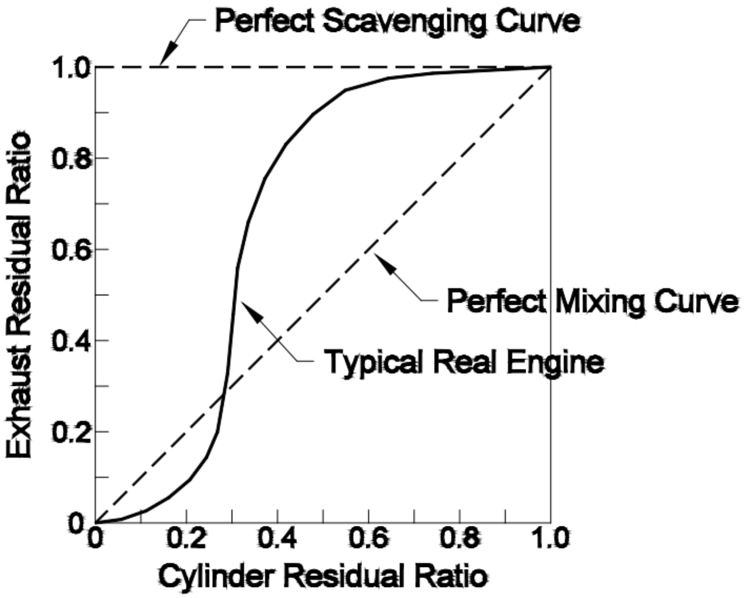

Figure 5: Perfect scavenging, perfect mixing, and typical real engine exhaust residual ratio vs cylinder residual ratio. Reprinted from [41]

When the fresh charge first begins to enter the cylinder, the cylinder and exhaust residual ratios will be unity. As more fresh charge enters the cylinder, the cylinder residual ratio will decrease. In real engines, the exhaust ratio remains close to one until the fresh mass can reach the outlet and cause the exhaust residual ratio to decrease. As the gas exchange process continues, short-circuiting causes the exhaust residual ratio to decrease to low levels. [41]

A CFD analysis can be conducted to determine the scavenging function, but it was not determined necessary for this project. Instead, a linear approximation of the Typical Real Engine line in Figure 5 was assumed.

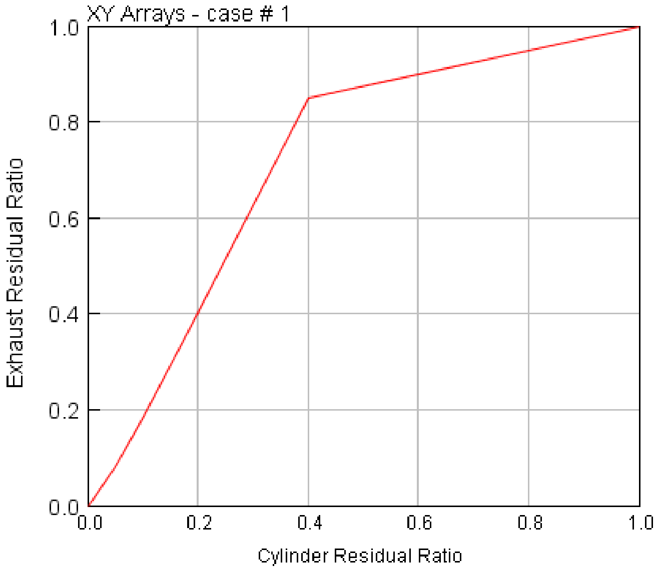

Figure 6: Scavenging model used in the engine simulation

2.4.5 Friction

A portion of the indicated work that is not available at the drive shaft is called friction work. Frictional losses can be divided into two major groups: friction between two lubricated metals in motion and turbulent dissipation. The first group mainly consists of bearings and the motion of the piston skirt against the cylinder liner. The second group involves the work required to pump fluids through flow restrictions such as air, coolant, and oil. [2]

The friction can be estimated using is the popular Chen-Flynn method. This is an empiric model to calculate the friction mean effective pressure (FMEP) as a function of peak cylinder pressure and mean piston speed. [50]

$$FMEP = C + (PF * P_{max}) + \left(MPSF * \overline{S_p}\right) + \left(MPSSF * \overline{S_p}^2\right) \tag{19}$$

Where C is the constant part of FMEP (the energy used by accessories, etc.), PF is the peak cylinder pressure factor (to account for load effects), P_{max} is the maximum cylinder pressure, $MPSF$ is the mean piston speed factor, $\overline{S_p}$ is the mean piston speed, and $MPSSF$ is the mean piston speed squared factor.

Total friction work per cycle has been shown to scale quadratically with engine speed. [2] It is preferred to estimate the friction in an engine by measuring the motoring torque using a dynamometer at a range of engine speeds. This is done by running the engine at steady state, cutting the fuel, and measuring the power necessary to maintain rpm. If using this method, it is important to factor in pumping and heat transfer losses to get an accurate friction estimate. However, this type of measurement is not possible for the engine of interest. Instead, the engine friction was estimated by using the measured cylinder pressure. [41] This was done by subtracting the measured indicated torque from the brake torque, and converting it into FMEP. Since there was no detailed information or data for this engine, the friction was assumed to be a constant 0.6 bar. Of course, there are inherent accuracy losses with this method, but because this engine typically runs at a constant speed, the frictional losses would not be expected to vary significantly. However, there are other sources of error such as measuring the indicated torque and cycle pressures varying between cylinders. [41]

2.4.6 Prechambers

Prechambers are small cylindrical volumes attached to the main chamber. They are used to extend the lean burn limit of the engine while also reducing cyclic variability. By doing so, they have been shown to reduce fuel consumption and reduce emissions [51] by creating a localized stoichiometric mixture near the spark plug to fully develop the flame kernel, and then jetting the hot partially burned mixture into the main chamber using a nozzle. The addition of turbulence and hot radical species helps combustion to stabilize and proceed through the rest of the mixture.

Many of the Cooper-Bessemer engines still in operation have been retrofitted with prechambers and electronic injection systems in order to meet the increasingly stringent emissions regulations. Typically, these prechambers are about 1 – 2% of the clearance cylinder volume.

2.4.7 Emissions Prediction

Emissions were not analyzed or evaluated in the model for this phase of the project, but the modeling fundamentals will still be discussed for completeness. GT-Power has the default capability of modeling the 13 main combustion products: N_2, O_2, CO_2, CO, H_2O, H_2, H, O, OH, NO, N, SO_2, and Ar. Predictive SI combustion models have the added ability to predict unburned hydrocarbons. Any or all of these models can be added to the model at a later date.

NO_x is calculated using the extended Zeldovich mechanism. This series of three chemical reactions is very sensitive to peak cylinder temperature and trapped cylinder mass, equivalence ratio, and combustion rate. [2]

CO_2, being a primary combustion product, is always included in emissions calculations.

CO is calculated using an equilibrium model but can also be determined using a kinetic model.

Unburned hydrocarbons can be calculated in two ways. The first way is to specify a crevice volume, and the hydrocarbons trapped in this volume at the end of combustion will remain unburned. The second option is to use a two plate quenching model and a simple kinetic model after the flame is quenched. Unburned hydrocarbons are calculated by estimating the amount of fuel and air mixture pushed into the crevice during the compression stroke that re-enters the cylinder in the expansion stroke. The mixture that enters the main cylinder volume before end of combustion is considered burned according to the combustion model. The mixture that enters the main cylinder after the end of combustion is burned according to the kinetic model. [41]

3. EXPERIMENTAL DATA COLLECTION

3.1 Natural Gas Composition Data Collection

Natural gas composition was tested using an on-site gas chromatograph and was recorded every hour from January 2016 to October 2016. This data was statistically analyzed to develop the natural gas mixtures for the chemical kinetic calculations later in this project.

The maximum, minimum, and average contents for some major species and a select few properties are shown in Table 2 and Table 3.

Table 2: Pipeline gas composition collected in 2016 on location. C4 includes IC4 and NC4 species. C5+ includes C5 and all heavier hydrocarbons

	C1 (mol%)	C2 (mol%)	C3 (mol%)	C4 (mol%)	C5+ (mol%)	CO_2 (mol%)	N_2 (mol%)
Max	93.87	9.3906	0.5882	0.1657	0.0916	0.80	0.44
Min	89.86	4.9966	0.2081	0.0146	0.0018	0.12	0.06
Avg	91.95	7.0886	0.3487	0.0687	0.0248	0.17	0.35
St. Dev.	0.54	0.5198	0.0596	0.0206	0.0078	0.04	0.02

Table 3: Pipeline gas properties collected in 2016 on location

	HHV (Btu/scf)	WI	SG
Max	1,085.5	1,394.33	0.6061
Min	1,048.2	1,361.27	0.5882
Avg	1,071.2	1,385.87	0.5974
St. Dev	4.8	3.03	0.0029

There is some variability in the gas composition throughout the 10 month period, but the composition swings are minimal compared to what has been seen at other locations in the U.S. as discussed in Section 2.2.1.2.

It is perhaps easier to visualize the 7,008 data points on a time basis. In Figure 7, the mole percentages of C1 and C2 are shown together. Note the different axes but same scales. Interestingly, it appears an increase in C1 corresponds with a decrease in C2 and vice versa. Figure 8 shows the fluctuation of N_2 and CO_2 over the same time period. In late April, there was a significant change in fuel composition. This is signified by the sudden decrease in C_2 and increase in CO_2. This increase in inerts is shown by a sharp decrease in HHV, shown in Figure 9. For completeness, the WI is shown in Figure 10.

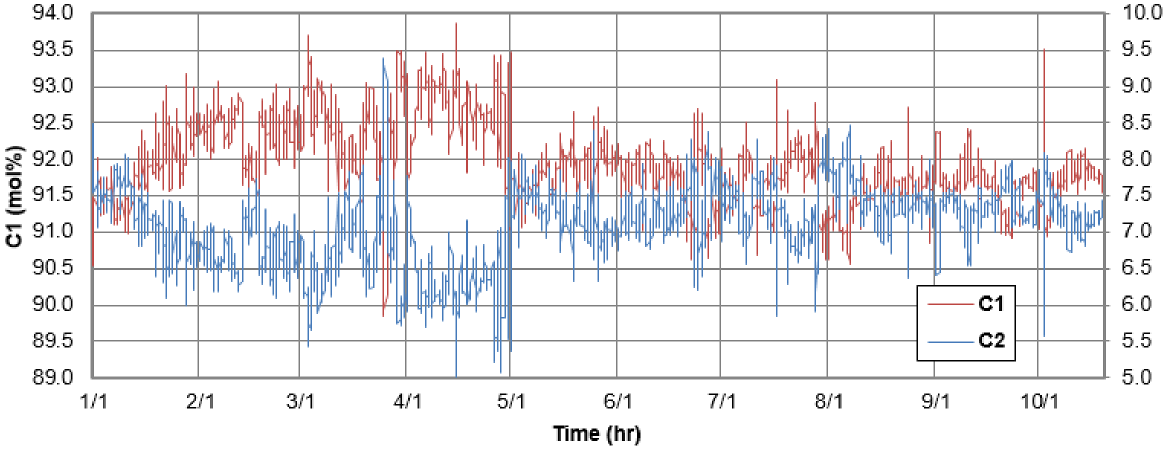

Figure 7: Variation of C1 and C2 on an hourly basis

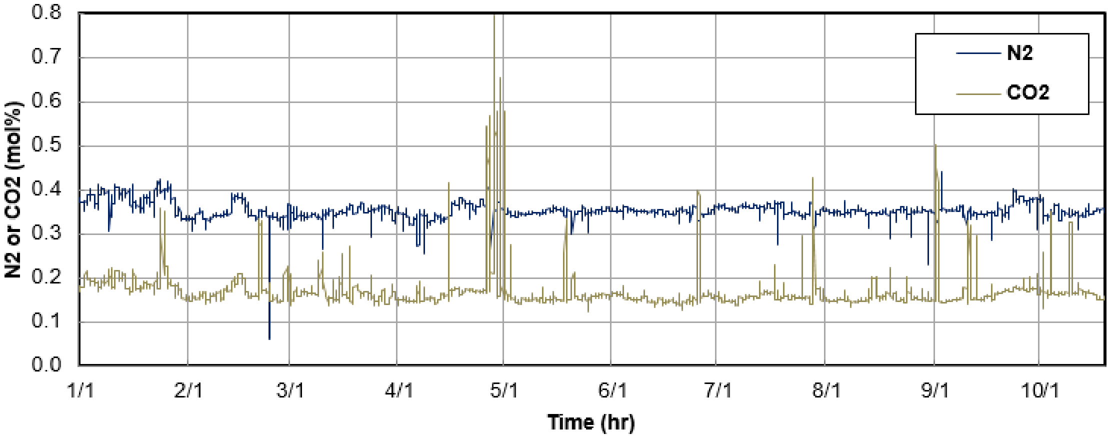

Figure 8: N2 and CO2 amounts in the fuel mixture at location

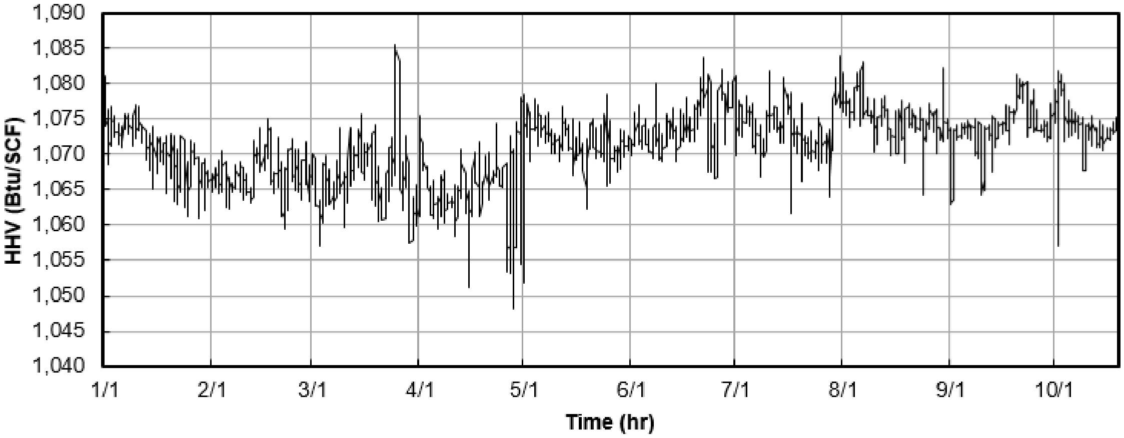

Figure 9: Fluctuation of HHV at location

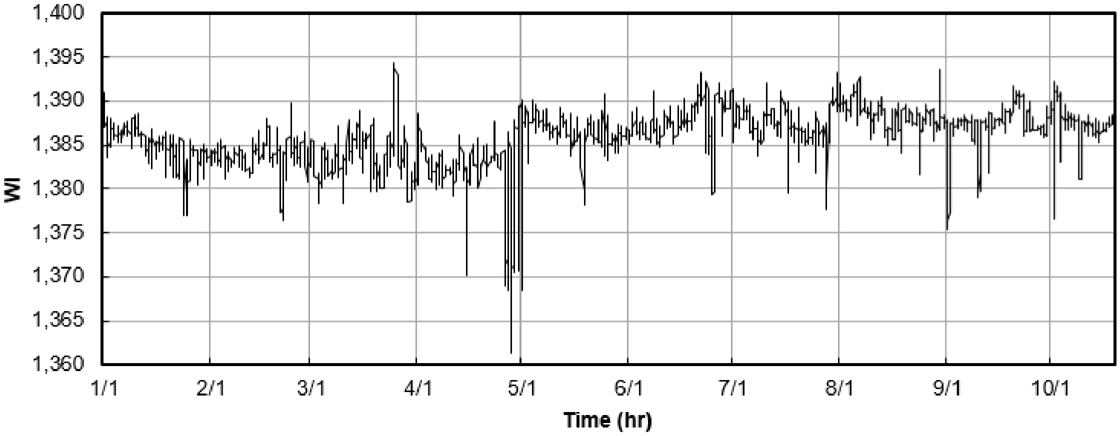

Figure 10: Fluctuation of Wobbe Index at location

Figure 11, which show C2 and C3 content versus C1, appears to support the earlier claim that C1 may lead to a proportional increase in C2. However, the changes in these two species cannot be directly related since the amounts of heavier hydrocarbons are also changing.

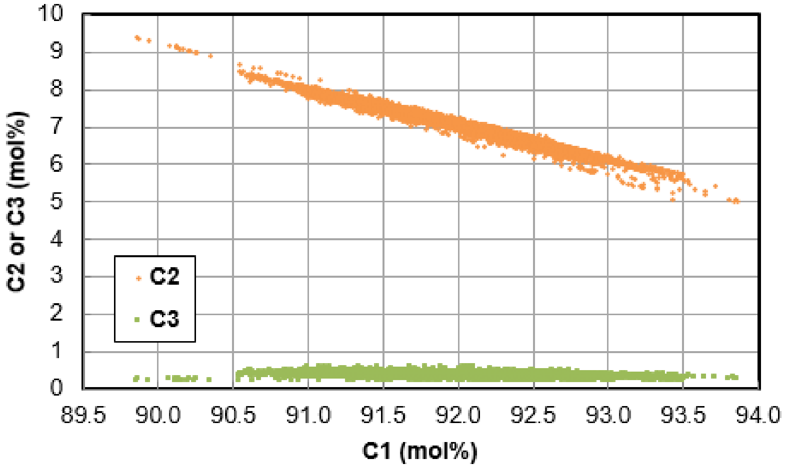

Figure 11: C2 and C3 amounts versus C1

Figure 12 shows HHV versus C1 content. Potentially, a preliminary relationship should be drawn between HHV and C1 content, but there are an increasing number of outliers as HHV decreases. The WI, shown in Figure 13, also has a similar trend as C1 content increases.

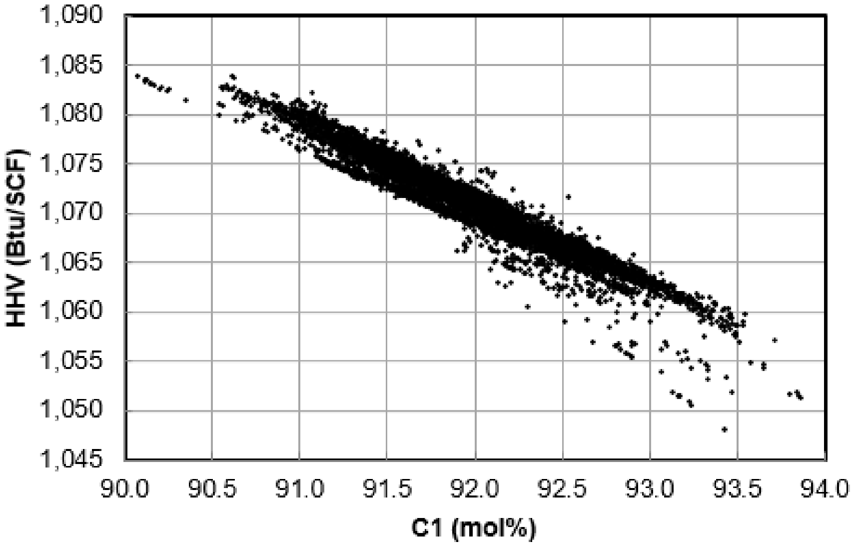

Figure 12: Higher heating value of the pipeline mixture versus C1 content

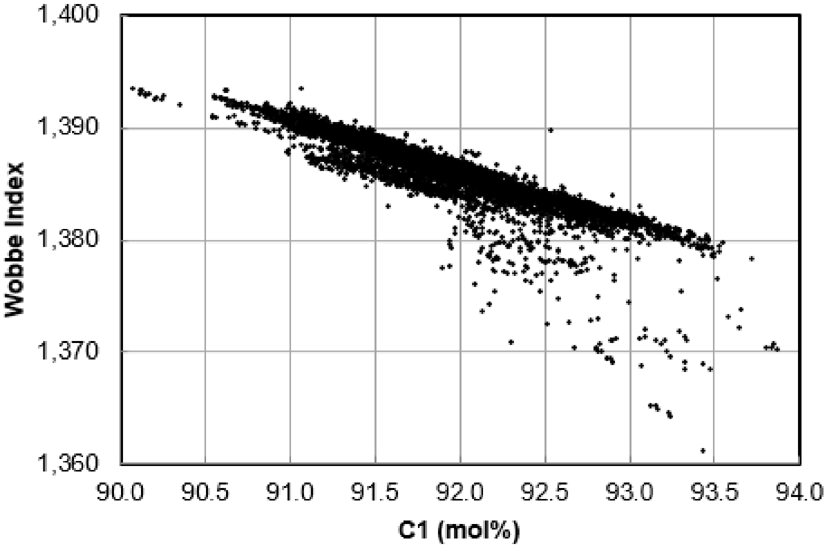

Figure 13: Wobbe index of the mixture versus C1 content

Using this data, the natural gas mixtures for the laminar flame speed and ignition delay study were defined. The average composition was used as the baseline cases, then each species was defined by individually adjusting the value to the maximum or minimum. In order to maintain a fractional sum of unity, the amount of methane was adjusted to make up the difference. This created a total of nine mixtures shown in Section 5.

3.2 Engine Data Collection

Simulation verification and validation requires experimental data. Therefore, the engine of interest was tested on-site by a third party, Advanced Engine Technologies Corporation. Over the course of two days, data was collected for a total of 17 operating conditions were tested. The Cooper-Bessemer GMWH-10C is rated for 3,400 bhp at 250 rpm. It has a nominal bore and stroke of 18” and 20”, respectively. This means the total displacement of the engine is about 834 L. Figure 14 shows the engine, and Table 4 summarizes the characteristics.

Figure 14: The engine of interest

Table 4: Engine Specifications

Make	Cooper-Bessemer
Model	GMWH-10C
Cycle	2
Rated HP	3,400
Rated Speed (rpm)	250
Number of Cylinders	10
Configuration	V-bank
Bore (inches)	18
Stroke (inches)	20

The load is represented as a percentage of rated engine torque (71,427 lbf ·ft). Normal operating conditions are considered 90% torque, 3.5 degrees before TDC

(°bTDC) ignition timing, and a trapped equivalence ratio (TER) of approximately 0.410. TER is a measure of the trapped mass air-fuel ratio. It takes into account the cylinder geometry, speed, air manifold pressure, air manifold temperature, the fuel flow, and fuel quality. It is considered a better metric for the real conditions and is a potential solution for closed-loop air-fuel ratio control. [52]

To define the test cases, load, ignition timing, and equivalence ratio were varied above and below the normal operating conditions. Engine speed was maintained at 250 rpm because it only changes under extreme circumstances or during startup and shutdown. Data collection was done by setting the desired input variables, waiting for the engine to reach steady-state, and then recording the data. Of these 17 runs, Run 4 most closely represents typical engine operation. Runs 1, 2, 6, 7, 12, 13, 16, and 17, shown shaded in the table below, were selected to verify the simulation by changing the torque, ignition timing, and TER around the baseline case. These cases were selected out of the other points because the data appeared to have less noise or scatter and overall appeared to better represent the system.

Table 5: Engine operating conditions

	Torque (%)	Ignition Timing (°bTDC)	TER
Run 1	76	3.5	0.399
Run 2	86	3.5	0.403
Run 3	83	3.0	0.400
Run 4	**91**	**3.5**	**0.410**
Run 5	91	4.0	0.405
Run 6	91	4.5	0.409
Run 7	90	5.0	0.410
Run 8	88	3.5	0.407
Run 9	89	3.0	0.410
Run 10	90	2.5	0.420
Run 11	96	3.5	0.408
Run 12	91	3.5	0.401
Run 13	90	3.5	0.378
Run 14	90	3.5	0.421
Run 15	91	3.5	0.466
Run 16	92	3.5	0.470
Run 17	84	2.0	0.401

The high speed data collected consists of crank-angle resolved in-cylinder pressure for each cylinder over 100 continuous cycles. There was a significant amount of noise in the pressure data caused by splitting the signal from the engine controller to the data acquisition system, so the sampling rate was increased to 6240 Hz to allow for post processing and filtering. The low speed data includes information on the horsepower output, the fuel and air flow rates, the intake manifold pressure and temperature, the turbocharger speed, and emissions such as dry O_2, dry NO, dry NO_x, dry CO, and THC.

The natural gas composition during the testing was also collected. Since the engine tests were conducted over two days, there is not a large change in gas composition. However, the location of this compressor station on the pipeline system suggests it may experience significant fuel composition fluctuations in the future.

Table 6: Summary of fuel composition during engine testing

Species	Maximum	Minimum	Average
Methane	0.933520	0.920491	0.925386
Ethane	0.069434	0.059883	0.064466
Propane	0.003737	0.002908	0.003198
Iso-Butane	0.000334	0.000262	0.000297
N-Butane	0.000341	0.000219	0.000287
Iso-Pentane	7.68E-05	4.88E-05	6.53E-05
N-Pentane	4.73E-05	2.48E-05	3.78E-05
Hexanes-plus	6.61E-05	3.41E-05	5.28E-05
CO2	0.001517	3.84E-05	0.001375
N2	0.003875	0.00372	0.003787

4. RESULTS: KINEMATIC MODELING[*]

The kinematic equations to express the motion of the power pistons of an articulated connecting rod were developed by understanding the movement as a simple linkage system shown in Figure 15. [53] The compressor is connected to the compressor (master) rod to the right.

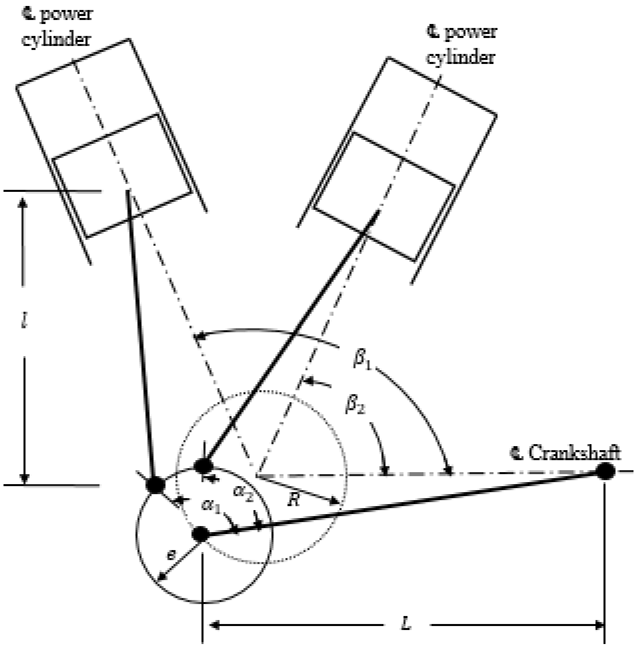

Figure 15: Geometry of the articulated connecting rod system. Reprinted with permission from [53]

Thus, an equation to express the piston pin location with respect to TDC, PP, as a function of the defined variables was developed.

---

[*] Reprinted with permission from "Kinematics of an articulated connecting rod and its effect on simulation compression pressures and port timings" by K. Fieseler, T. Jacobs, and M. *Patterson, 2018. ASME Journal of Engineering for Gas Turbines and Power, 140(9).* Copyright 2018 by ASME.

$$PP = R\cos\theta + e\sin\left(\alpha - \arcsin\left(\frac{R\sin(\beta-\theta)}{L}\right)\right) + \sqrt{l^2 + \left(R\sin\theta + e\cos\left(\alpha - \arcsin\left(\frac{R\sin(\beta-\theta)}{L}\right)\right)\right)^2} \tag{20}$$

where R is the crank throw radius, θ is the crank angle, e is the hinge pin offset from the crank, β is the angle from the crankshaft centerline to the power cylinder centerline, L is the compressor (master) rod length, l is the piston connecting rod length, and α is the angle from the compressor rod to the hinge pin.

Similarly, the piston motion was derived for a normal crank train, which is just a slider-crank mechanism shown in Figure 16.

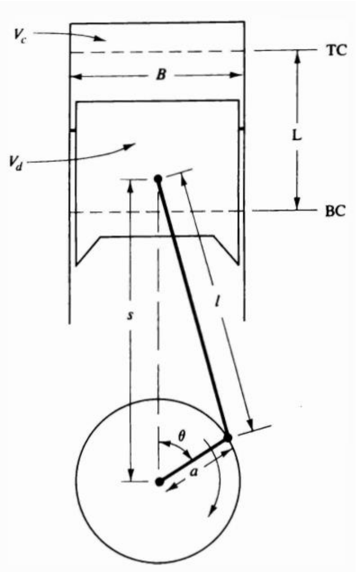

Figure 16: Geometry of a typical crank train. Reprinted from [2]

The distance from the crank axis to the piston pin, s, can be expressed by

$$s = a\cos\theta + \sqrt{l^2 - (a\sin\theta)^2} \tag{21}$$

where a is the crank radius, θ is the crank angle, and l is the connecting rod length. In order to compare this expression with Equation (20), the origin must be shifted from the crank axis to the TDC of the cylinder. This results in the following equation.

$$PP_{sc} = a + l - (a\cos\theta + \sqrt{l^2 - (a\sin\theta)^2}) \tag{22}$$

4.1 Piston Profiles

Now it is straightforward to compare the linkage systems. Equation (20) was used to calculate the piston motions for all four of the compressor-piston configurations, and Equation (23) was used to calculate the piston motion for a slider crank mechanism. RH corresponds to the right hand side of the engine, while LH corresponds to the left hand side.

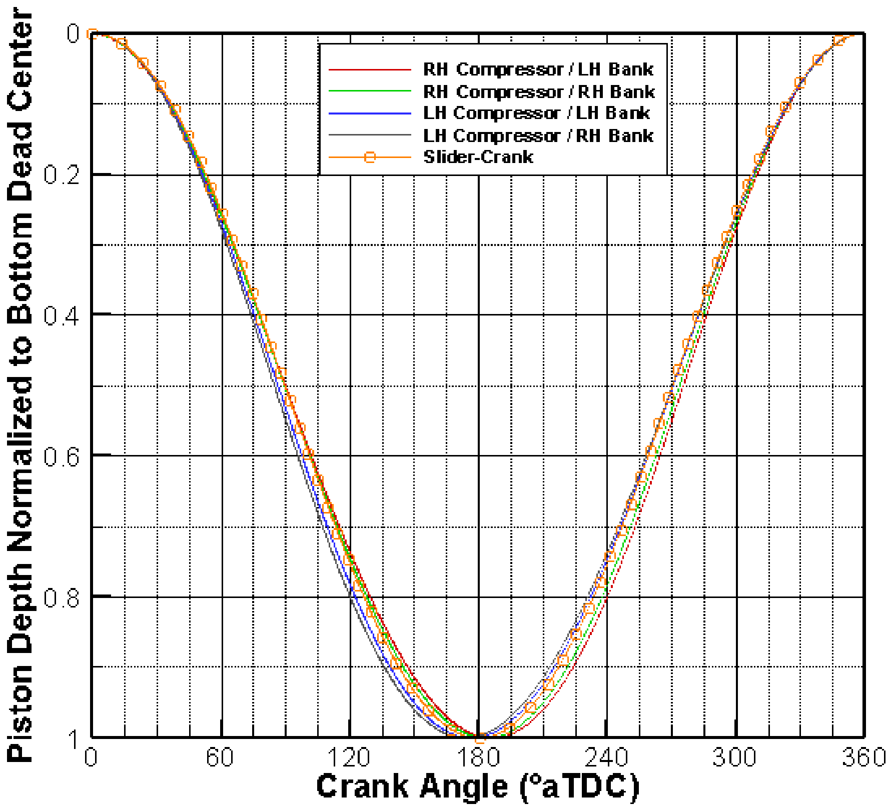

Figure 17: Piston depth profile normalized to BDC for all conditions. Reprinted with permission from [53]

The left side of Figure 17 begins with all pistons at their respective (local) TDC. This is the point when the piston is at the highest location in the cylinder and the piston has its lowest volume. As the crank shaft rotates, each configuration has a slightly different profile. A zoomed-in diagram is shown in Figure 18.

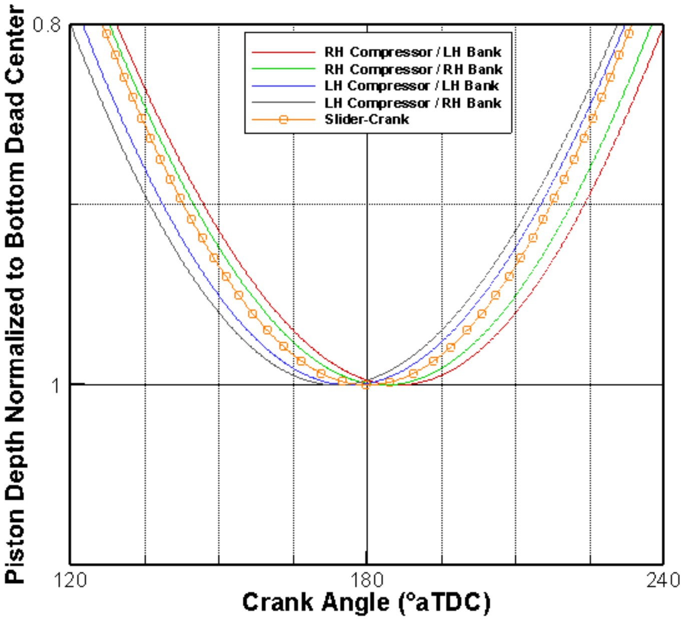

Figure 18: Piston depth profile normalized to BDC for all conditions, zoomed in. Reprinted with permission from [53]

The LH compressor / RH bank is the most advanced, followed by the LH compressor / LH bank piston. These two reach BDC slightly before 180 CAD rotation from TDC. The most delayed is the RH compressor / LH bank, followed by the RH compressor / RH bank piston. These two configurations reach TDC slightly after 180 CAD rotation from TDC. The slider-crank mechanism is between the LH compressor / LH bank and the RH compressor / RH bank, and it is perfectly symmetric around BDC – it is the only configuration in which BDC corresponds to exactly 180 CAD from TDC as expected.

The cause of this change is due to the hinge pin offset creating an elliptical shape instead of circular. The size of this ellipse depends on the geometry of the linkage system. In order to properly show the hinge pin motion with respect to its center of rotation, Figure 19 and Figure 20 are normalized with respect to the motion in both the horizontal and vertical directions.

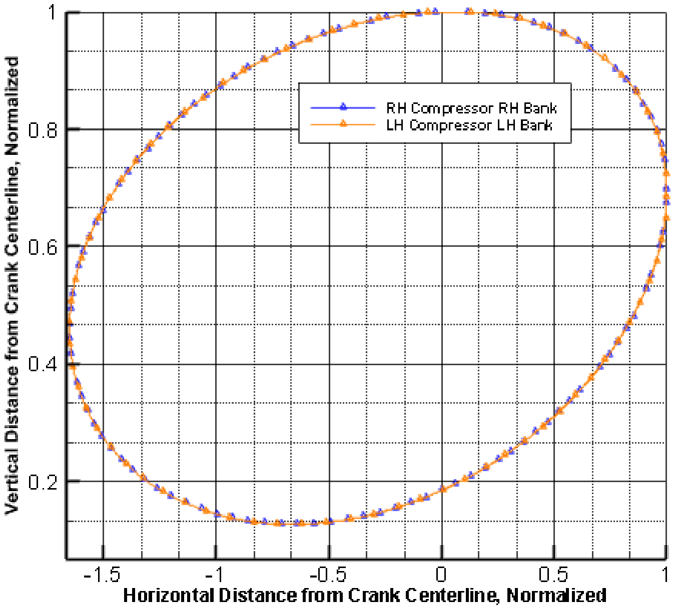

Figure 19: Normalized hinge pin motion for pistons with same-side compressors. Reprinted with permission from [53]

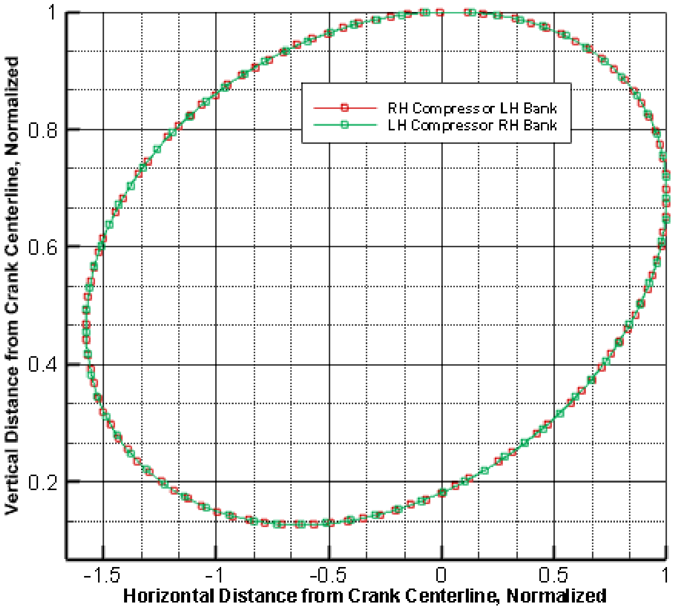

Figure 20: Normalized hinge pin motion for pistons with opposing-side compressors. Reprinted with permission from [53]

All hinge pins have the same vertical displacement. The hinge pins located on the same side as the compressor experience more horizontal displacement causing those cylinders to have a slightly longer stroke. This longer stroke is what causes slightly higher geometric compression ratios reported in previous studies.

4.2 Port Timing

Next, the profiles shown in Figure 17 were used to determine the port timings for each compressor/piston configuration. It was assumed the ports inside each cylinder had the same shape and were located the same distance from the top of the cylinder. The effects of manufacturing tolerance for both the cylinders and cylinder liners were neglected – a reasonable assumption considering it would be around +/- 1/16”. Given this location, the opening and closing of the intake and exhaust ports were determined respective to the slider-crank mechanism. Positive values correspond to delays or retardations, and negative values correspond to early timings or advancements.

Table 7: Intake and exhaust port timings compared to the slider-crank mechanism

	EPO	IPO	IPC	EPC
RH comp / LH bank	7	10.2	0	0.8
RH comp / RH bank	6	8.6	-2.8	-1.6
LH comp / LH bank	1.6	2.8	-8.6	-6
LH comp / RH bank	-0.8	0	-10.2	-7

This information can be represented in a bar chart for easier understanding.

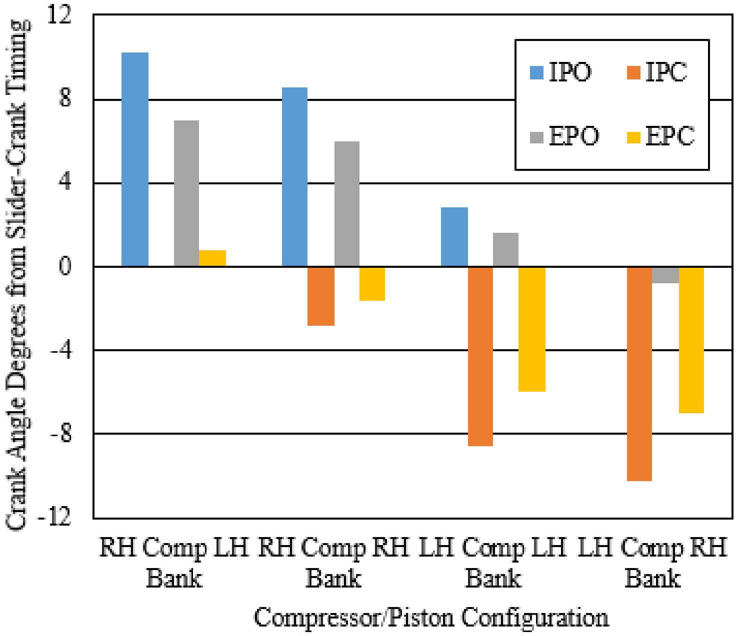

Figure 21: Intake and exhaust port timings compared to the slider-crank mechanism. Reprinted with permission from [53]

The asymmetric piston motion also causes asymmetric port opening and closing. The RH compressor / LH bank piston, having the most delayed piston profile, also has the most delayed port timings while the LH compressor / RH bank piston, having the most advanced profile, also has the most advanced port timings.

For a RH compressor / LH bank piston, IPC occurs at the same time for the slider-crank, but IPO is 10 CAD later. Additionally, EPC is within 1 CAD, but EPO is 7 CAD retarded. The is reversed for the LH compressor / RH bank, which has IPC occurring 10 CAD early and EPC occurring 7 CAD early.

For a RH compressor / RH bank piston, IPO is 8.6 CAD retarded, IPC is about 3 CAD early, EPO is 6 CAD retarded, and EPC is about 1.6 CAD early from slider-crank timing. For the LH compressor / LH bank, IPO is 3 CAD delayed, IPC is 8.6 CAD early, EPO is 1.6 CAD late, and EPC is 6 CAD early. It is this effect of the ports opening later and closing earlier that lend to the higher geometric compression ratios. This effect is complimentary to these pistons having a slightly longer stroke.

The timing and exposed areas of the intake and exhaust ports affects the in-cylinder scavenging by affecting the air flow. This can change the overall gas motion between the intake manifold, the cylinder, and the exhaust manifold to either enhance or hinder scavenging efficiency and scavenging ratios. This information will be used in the full-scale engine model of the GMW.

5. RESULTS: LAMINAR FLAME SPEED AND IGNITION DELAY

The LFS and ID test spaces were developed by considering the range of natural gas composition at the location of interest, typical engine operating conditions, and limitations of the chemical kinetic mechanism. The test fuel mixtures were determined according to the actual compositions seen on location in 2016 (discussed in Section 3.1). The average composition was taken to be the baseline case. The other eight mixtures were developed by individually adjusting each species content to the maximum or minimum value seen during the 10 month period, and then changing C1 to maintain a fractional sum of unity. The composition of the nine total mixtures is shown in Table 8.

Table 8: Fractional compositions of the nine fuel mixtures

	C1	C2	C3	C4	C5
Average	0.92430	0.07126	0.00350	0.00069	0.00025
C2high	0.90535	0.09021	0.00350	0.00069	0.00025
C2low	0.94300	0.05256	0.00350	0.00069	0.00025
C3high	0.92215	0.07126	0.00565	0.00069	0.00025
C3low	0.92561	0.07126	0.00219	0.00069	0.00025
C4high	0.92340	0.07126	0.00350	0.00159	0.00025
C4low	0.92484	0.07126	0.00350	0.00015	0.00025
C5high	0.92367	0.07126	0.00350	0.00069	0.00088
C5low	0.92453	0.07126	0.00350	0.00069	1.89e-5

The chemical mechanism used was developed and validated by the Combustion Chemistry Centre at the National University of Ireland in Galway. Referred to as nc5_49, it contains 293 species and 1,588 reactions. [54] Computation time increases with mechanism size, and this was the largest mechanism that contained the species of interest without being too large. While the chemical mechanism has been validated, preliminary mixtures were tested in order to ensure proper implementation and correct Cantera Python coding. These mixtures and their initial conditions were determined from experimental published data shown in A.1.

5.1 Laminar Flame Speed Curve Fitting

When the flame propagates through the cylinder, temperature and pressure increase. Under typical operating conditions for the engine of interest, this means temperatures as high as 1,800 K and pressures as high as 45 bar. Laminar flame speeds were initially calculated at these extreme conditions, but they were considered unreliable due to limitations with the chemical kinetic mechanism. Therefore, the temperature was restricted to a maximum of 700 K and a pressure of 40 bar. This is a lean-burn engine, so typical equivalence ratios are near stoichiometric in the prechamber and very lean in the main chamber (around 0.4). The range of equivalence ratios is large, but most of the values are near the extremes. For large bore two-stroke engines, the residual fraction is typically around 10%, so the range from 0% to 20% was included. The moderate conditions (300 K, 1 bar, and 0% residual fraction) are not directly engine relevant, but were included for LFS and chemical mechanism validation. The final test matrix is shown in Table 9.

Table 9: Laminar flame speed test space

Variable	Range	Values
Temperature [K]	300 – 700	Steps of 200
Pressure [bar]	1 – 40	Steps of 10
Equivalence Ratio	0.4 – 1.2	0.4, 0.45, 0.5, 0.55, 0.7, 0.75, 0.8, 0.9, 1.0, 1.1, 1.2
Residual Fraction	0 – 0.2	Steps of 0.1

A total of 4,455 LFS were calculated. After running this calculations, the equation from Metghalchi and Keck [38] was generalized as a function of mixture composition. This was done by expanding the original coefficients to be variables of mixture composition.

$$\begin{aligned} B_m = B_{m00} + B_{m11}X_{C1} + B_{m21}X_{C2} + B_{m31}X_{C3} + B_{m41}X_{C4} + B_{m51}X_{C5} \\ + B_{m12}X_{C1}^2 + B_{m22}X_{C2}^2 + B_{m32}X_{C3}^2 + B_{m42}X_{C4}^2 \\ + B_{m52}X_{C5}^2 \end{aligned} \tag{23}$$

$$B_\phi = B_{\phi 0} + B_{\phi 1}X_{C1} + B_{\phi 2}X_{C2} + B_{\phi 3}X_{C3} + B_{\phi 4}X_{C4} + B_{\phi 5}X_{C5} \tag{24}$$

$$\alpha = \alpha_A + \alpha_B(\phi - \alpha_C)^2 \tag{25}$$

$$\begin{aligned} \beta = \beta_{00} + \beta_{11}\mathrm{X}_{\mathrm{C1}} + \beta_{21}X_{C2} + \beta_{31}X_{C3} + \beta_{41}X_{C4} + \beta_{51}X_{C5} + \beta_{12}X_{C1}^2 \\ + \beta_{22}X_{C2}^2 + \beta_{32}X_{C3}^2 + \beta_{42}X_{C4}^2 + \beta_{52}X_{C5}\text{^}2 + \beta_B(\phi - \beta_C)^2 \end{aligned} \tag{26}$$

$$Dilution = 1 - 0.75 * D(1 - (1 - 0.75 * D * X_{res})^7) \tag{27}$$

The coefficients were calculated by fitting coefficients to a random selection of half of the data points, and then calculating the error when the line was fit to all of the points. The final equation has 34 variables. The values for the coefficients are shown in Table 10.

Table 10: Values for the coefficients in the generalized LFS equation

Coefficient	Value
B_{m00}	14.8521318623875
B_{m11}	-15.5556228150971
B_{m21}	-13.1273151341155
B_{m31}	-13.1578594199685
B_{m41}	-13.5491204529893
B_{m51}	-13.6189106069953
B_{m12}	1.08929356556684
B_{m22}	-2.03189003048173
B_{m32}	-26.4436264477547
B_{m42}	-90.2705391705801
B_{m52}	-537.591078301868
$B_{\phi 0}$	3.8833845955
$B_{\phi 1}$	-4.623203810
$B_{\phi 2}$	-4.888207855
$B_{\phi 3}$	-6.689029824
$B_{\phi 4}$	-2.788789507
$B_{\phi 5}$	-13.60081756
α_A	1.7706558456
α_B	0.3243753989
α_C	0.7714523225
β_{00}	-0.959755635
β_{11}	4.4121880682
β_{21}	5.5867637718
β_{31}	13.653910010
β_{41}	22.066969374
β_{51}	4.7458216256
β_{12}	-0.313265019
β_{22}	-974.0765741
β_{32}	-9217.631145
β_{42}	-3150.476399
β_{52}	-4.550872598
β_B	1.0133280208
β_C	-11.03253467
D	0.3268

This equation has a root mean square error (RMSE) of 0.044 m/s.

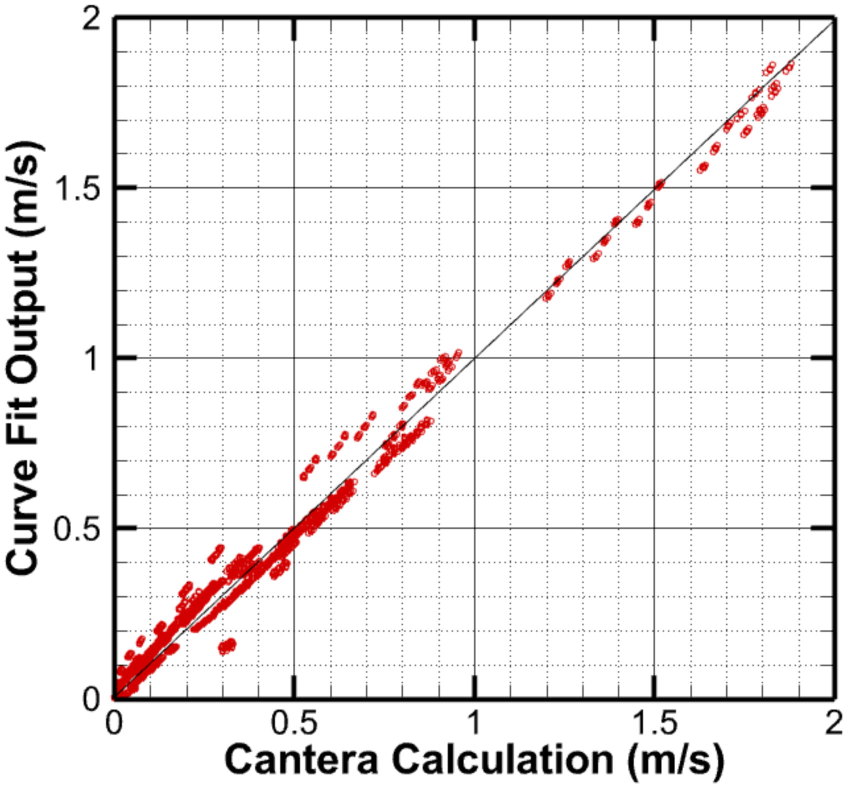

Figure 22: Curve fit output versus Cantera Calculation

To achieve this fit, several different methods were attempted such as splitting up the data into three equivalence ratio ranges, separating the data by residual fraction, and expanding the equation to have parabolic functions of specie composition. The first resulted in a better RMSE but would be much more difficult to implement in engine simulation. The second did not improve the overall fit. The third method resulted in a better RMSE, but it was an overfit and thus not a good representation of the whole data set.

Parabolic expressions were determined for the temperature and pressure exponents. In agreement with Metghalchi and Keck's work, in addition to that of Hedrick, the temperature exponent is not a function of mixture composition. [38] [45]

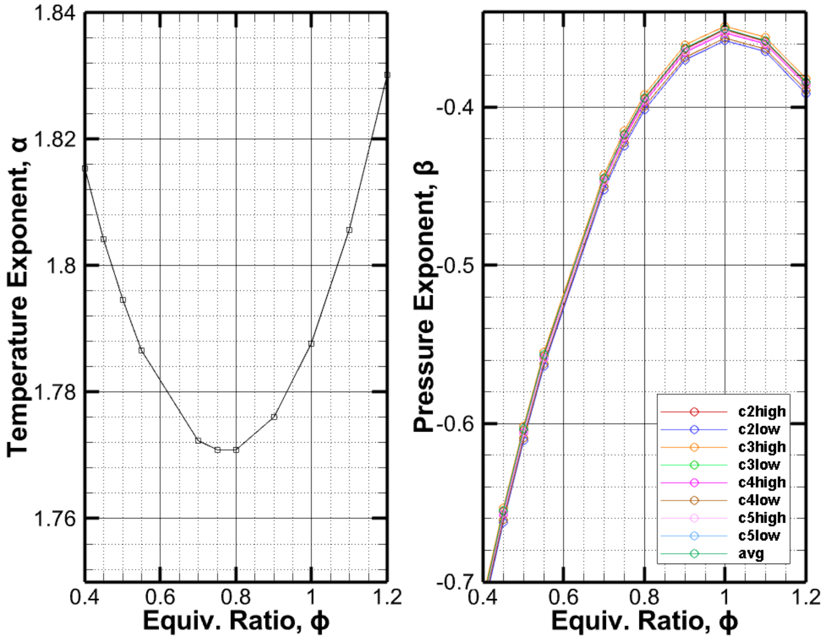

Figure 23: (Left) Temperature exponent versus equivalence ratio. (Right) Pressure exponent versus equivalence ratio for all mixtures.

Equivalence ratio sweeps at two conditions were compared to show how the fit represents the actual data. The first set of conditions are at T_{ref} and P_{ref} (298 K and 1 bar) and 0% residual fraction to see how the low temperature and pressure conditions compare.

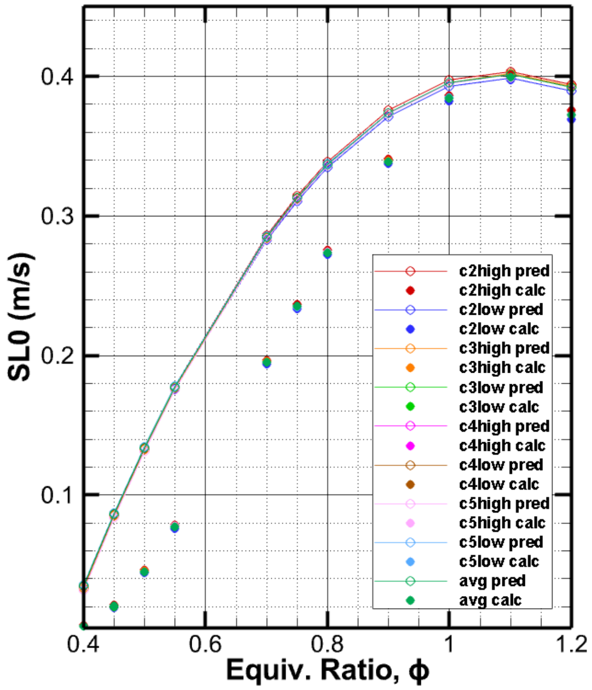

Figure 24: LFS vs equivalence ratio for predicted and calculated values at 298 K, 1 bar, and 0% residuals

The maximum percent difference for this set of conditions is about 100% more than the calculated value. However, there is a better fit for near-stoichiometric conditions. Additionally, the LFS for all mixtures converge for the entire equivalence ratio range. There is a better match at engine-relevant conditions.

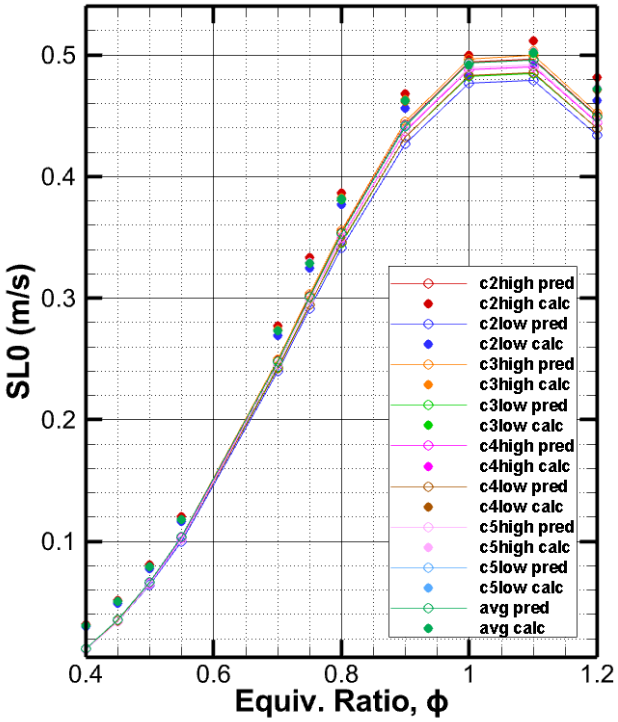

Figure 25: LFS vs equivalence ratio for predicted and calculated values at 700 K, 40 bar, and 0% residuals

The predicted value is about 8% lower than the calculated value, and overall it is a good match for the engine equivalence ratio range. The LFS of these mixtures converge at low equivalence ratios, but diverge as the mixture becomes richer.

In order to quantify the relative impact of a variable on LFS, a sensitivity analysis was conducted. The sensitivity quantifies the relative impact a certain variable will have on the target variable. A percent positive value represents the likelihood increasing this variable will increase the target variable by the amount in the positive magnitude column. Similarly, the percent negative value is the likelihood increasing the variable will decrease the target value by the amount in the negative magnitude column.

Table 11: Sensitivity study conducted for the LFS equation

Variable	Sensitivity	Percent Positive	Positive Magnitude	Percent Negative	Negative Magnitude
P	0.576	0	0	100	0.5763
Phi	0.555	90	0.5954	10	0.1883
T	0.4012	100	0.4012	0	0
Xres	0.0226	0	0	100	0.0226
XC1	0.2211	0	0	100	0.2211
XC2	0.1908	100	0.1908	0	0
XC3	0.0205	100	0.0205	0	0
XC4	0.0071	100	0.0071	0	0
XC5	0.0065	100	0.0065	0	0

From the sensitivity study, it is clear that the initial pressure, equivalence ratio, and initial temperature have the most significant impact on the LFS. The methane fraction has the biggest impact of the mixture species, followed closely by ethane. The LFS is about 10 times less sensitive to propane than methane or ethane, and even less sensitive to the amounts of butane or pentane. This could be due to the low amount of higher hydrocarbons and the small changes between the mixtures, or because the changing about of a HHC species was adjusted for in the amount of methane. More likely, these results show that propane, butane, and pentane do not have a significant impact on the total LFS of an alkane mixture when compared to the effect of pressure, equivalence ratio, and temperature.

5.2 Ignition Delay Curve Fitting

The chemical ignition delay of the fuel mixture is not directly related to the combustion calculations within the engine simulation software. Because this is a spark ignition engine, combustion is simulated to begin at the spark timing regardless of the chemical properties, so end-gas auto ignition, or knock, is not a major concern. Therefore, a detailed analysis of ignition delay was not conducted, but a preliminary equation was developed.

The ID test matrix was developed in a manner similar to that of the LFS. The nine mixtures are the same, the initial pressures are the same, but the initial temperature range was increased. The highest equivalence ratio was decreased from 1.2 to 1.15 to better distribute the points. Additionally, more temperature points were tested because ignition delay is heavily dependent on initial temperature. Only five equivalence ratios were tested in order to reduce the size of the test matrix.

Table 12: ID test space

Variable	Range	Values
Temperature [K]	1100 – 2000	Steps of 100
Pressure [bar]	1 – 40	Steps of 10
Phi	0.4 – 1.15	0.4, 0.65, 0.9, 1.0, 1.15
Residual Fraction	0 – 0.2	Steps of 0.1

A total of 6,750 cases were tested. However, at certain low temperature and low pressure conditions, the solution did not converge in the allotted time, so these cases were discarded. Ultimately, there were 5,045 ignition delay times. The data was then fit to the Douaud and Eyzat [44] equation.

$$\tau = \beta_1 \left(\left(\frac{1}{\phi} \right)^{\beta_5} \frac{MN}{100} (1 - \beta_6 X_{res}) \right)^{\beta_2} P^{\beta_3} \exp(\frac{\beta_4}{T}) \tag{28}$$

With coefficients defined as follows

Table 13: Coefficients fit to the ignition delay equation

Variable	Value
β_1	0.000139586772310659
β_2	3.30715924742344
β_3	-0.544664856163752
β_4	13401.6771014772
β_5	0.092778498622638
β_6	-0.0278749822715228

This results in an overall fit with an RMSE of 0.098 ms. The previous fit developed by Hedrick for binary methane and ethane mixtures resulted in an RMSE of 0.125 ms. [45] This fit is better, but it can still be improved. A visual representation of the Cantera data compared to the curve fit output is shown in Figure 26. The diagonal line shows the 1:1 ratio.

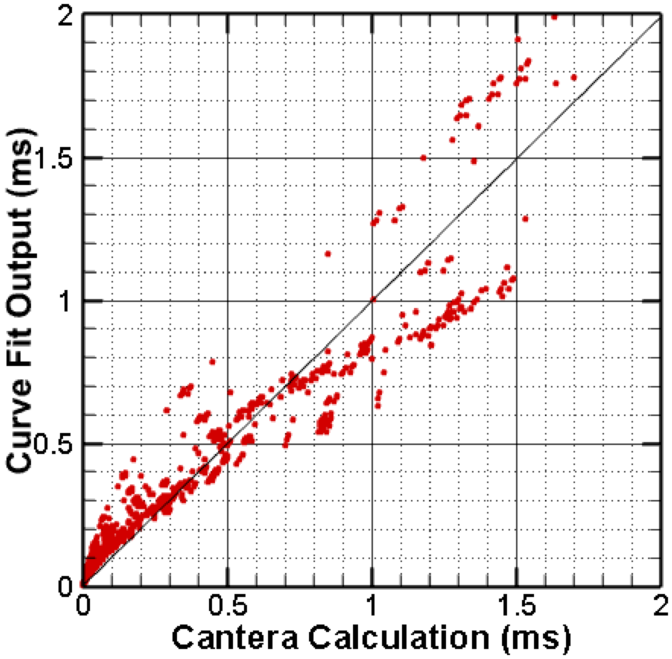

Figure 26: Curve fit output vs Cantera calculated value for the ID test space.

A sensitivity study was also conducted in order to quantify the relative impact of the independent variables.

Table 14: Results of the sensitivity study for ID

Variable	Sensitivity	Percent Positive	Positive Magnitude	Percent Negative	Negative Magnitude
T	4.7738	0	0	100	4.7738
P	1.121	0	0	100	1.121
Phi	0.076006	0	0	100	0.076006
MN	0.039957	100	0.039957	0	0
Xres	0.0044938	100	0.0044938	0	0

Increasing initial temperature, initial pressure, and equivalence ratio will always decrease ID, while increasing the MN or residual fraction will decrease the ID – this is known and accepted. However, what these results also show is the impact a change in any of these variables will have on ID. The ID is most sensitive to the initial temperature, but it is also sensitive to initial pressure. The equivalence ratio, MN, and residual fraction, while still influencing the ID, do not have a significant impact compared to the other variables.

6. RESULTS: GT-POWER

The GT-Power model includes the piston motion and port profiles calculated earlier in the project, two prechambers for each cylinder, and a turbocharger and intercooler. This model was built by starting with a working model of an open-chambered GMV and implementing GMW geometry and information provided by Baker Hughes, a GE Company, and Enbridge, Inc. Certain coefficients for the heat transfer, discharge, and turbulent flame speed were tuned for normal engine operating conditions and re-evaluated at extreme conditions.

6.1 Prechamber Modeling

The prechambers were modeled in GT-Power as simple cylinder objects with a stationary piston with an orifice between the two chambers to act as the nozzle. The orifice allows for pressure continuity and mass transfer, but the chemistry solver within the software is not robust enough to account for the propagation and termination of radicals in the partially burned mixture. Because of this, an addition spark plug had to be included in the main chamber to allow combustion to fully propagate. Figure 27 shows the prechamber model. The full engine model is shown in A.2.

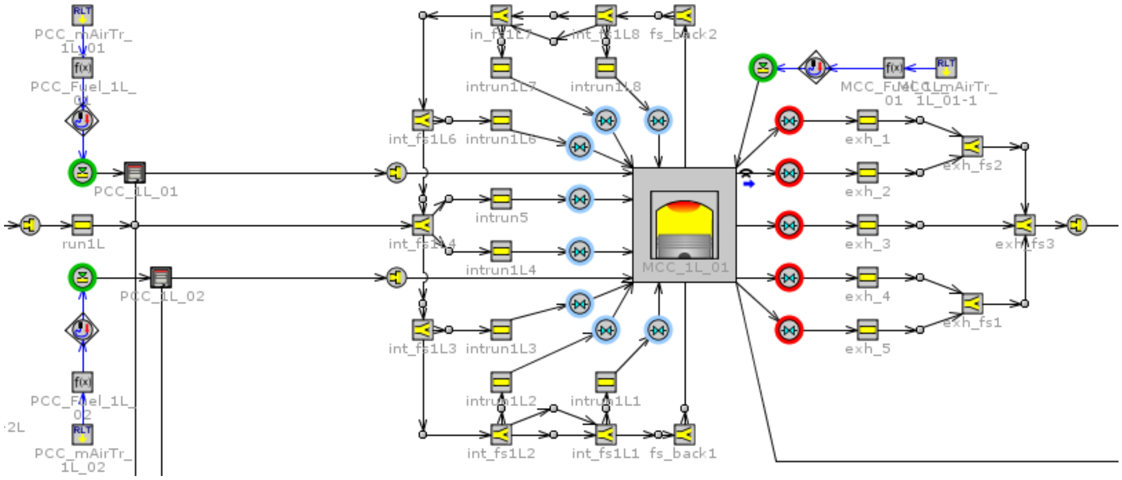

Figure 27: Diagram of the GT-Power model showing one main chamber with two prechambers connected

There was no experimental data collected for the prechambers, so actual fueling or pressure is unknown. Thankfully, previous studies have looked at the same prechambers in a Cooper-Bessemer GMV, and the results can be compared to the modeled pressures. Since this type of prechamber is designed to operate at stoichiometric conditions, a simple calculator was implemented into the model that calculates the fuel mass from the trapped air and the stoichiometric air-fuel ratio of the fuel. For the baseline operating case, this amount to close to 15 mg of fuel or 0.5% of total cylinder fueling.

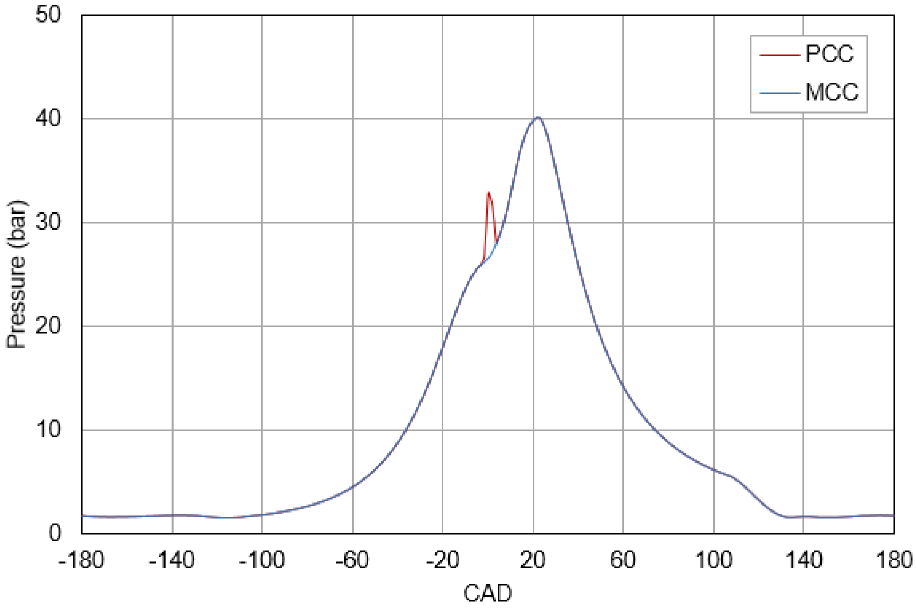

Figure 28: Prechamber pressure and main chamber pressure for Run 4 of Cyl 1L

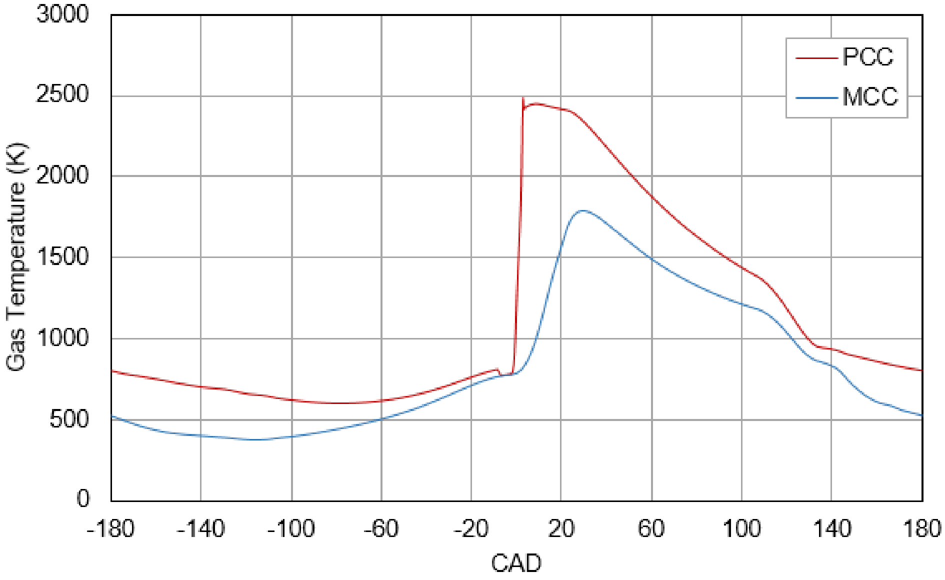

Figure 29: Temperature of prechamber and main chamber for Run 4 of Cyl 1L

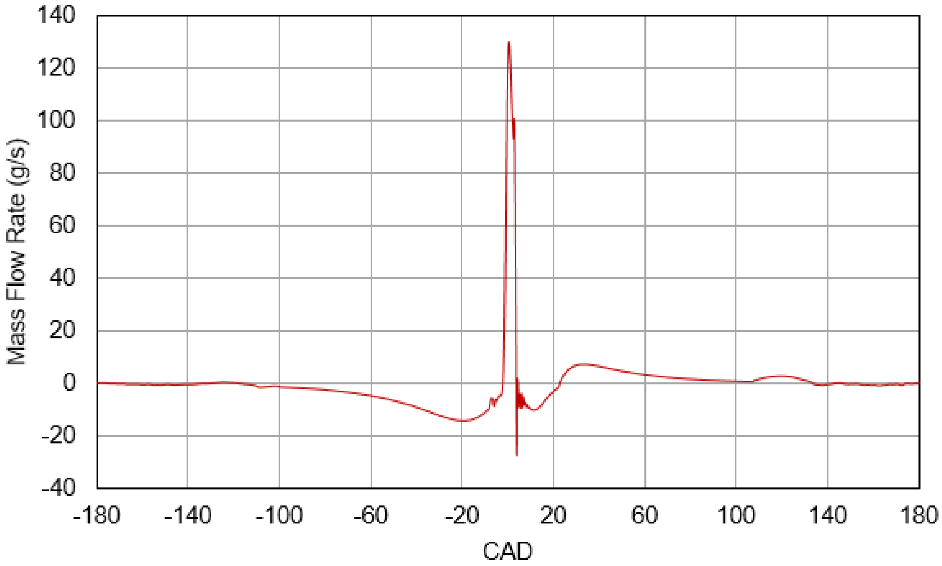

Figure 30: Mass flow rate out of prechamber for Run 4 of Cyl 1L

The chamber pressure was compared with data collected from a similar engine [55] with good results. The gas temperature and mass flow rates appear to be reasonable, and comparing these values with other experimental work could be done at a later date once such data is available.

6.2 Model Verification and Validation

Combustion tuning was done by adjusting the flame kernel growth multiplier, the turbulent flame speed multiplier, and the Taylor length scale multiplier until peak pressures and IMEPs of the cases were within +/- one standard deviation from the experimental data average. The average IMEP was calculated by averaging the IMEP of the 1,000 individual cycles. The location of peak pressure was a close enough match for all the cases, so it was not compared directly but could be done at a later date. The model showed a good match for all of the seven test cases selected for verification. The pressure trace for Run 4 is shown in Figure 31. The average experimental pressure trace for each cylinder is shown as a grey dotted line, and the simulation pressures are shown as solid colored lines. The engine average peak pressure is shown as a dashed horizontal line and is flanked on both sides by dashed lines representing +/- one standard deviation.

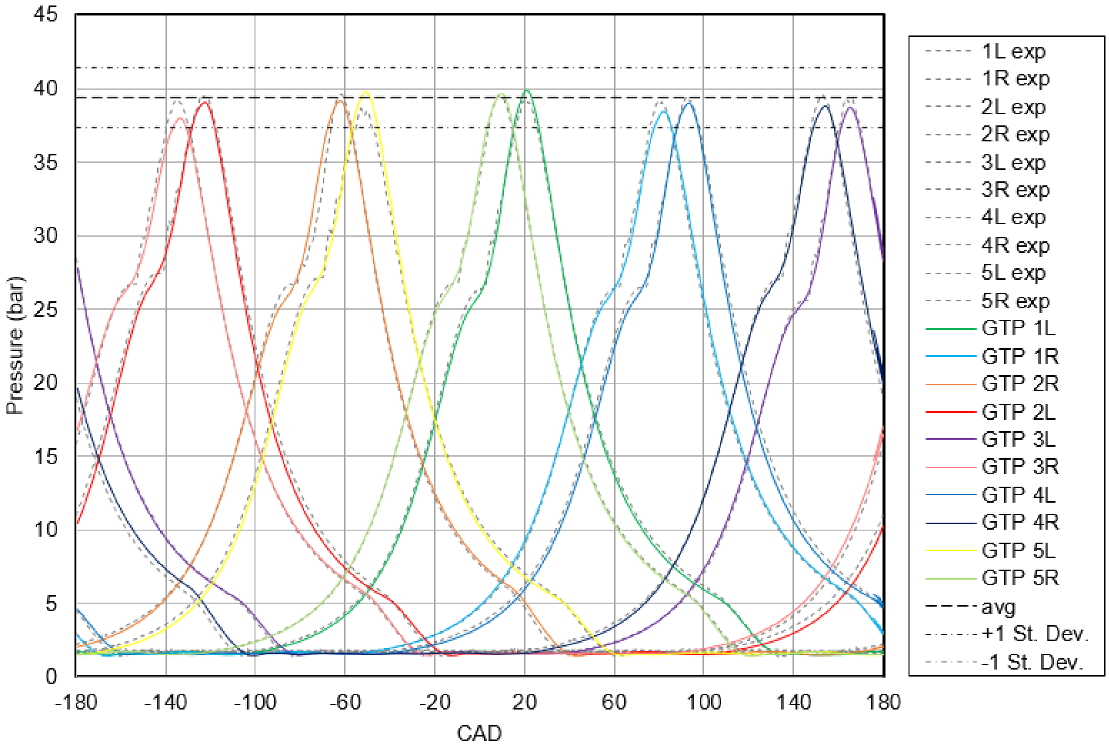

Figure 31: Pressure trace comparing simulation of prechambered model to experimental case over one flywheel revolution for Run 4

Throughout the cycle, there is a good match of pressures. For some cylinders, 2R for example, there is some difference in peak compression pressure. This could be due to a minor discrepancy in the effective compression ratio or trapped mass. There are also some differences in the power strokes that could be attributed to the Woschni model being inaccurate in the heat transfer calculations.

The pressure traces for the other cases are shown in A.3. The remaining case, Run 13, was the leanest operating case and perhaps the hardest to tune. It is shown in Figure 32.

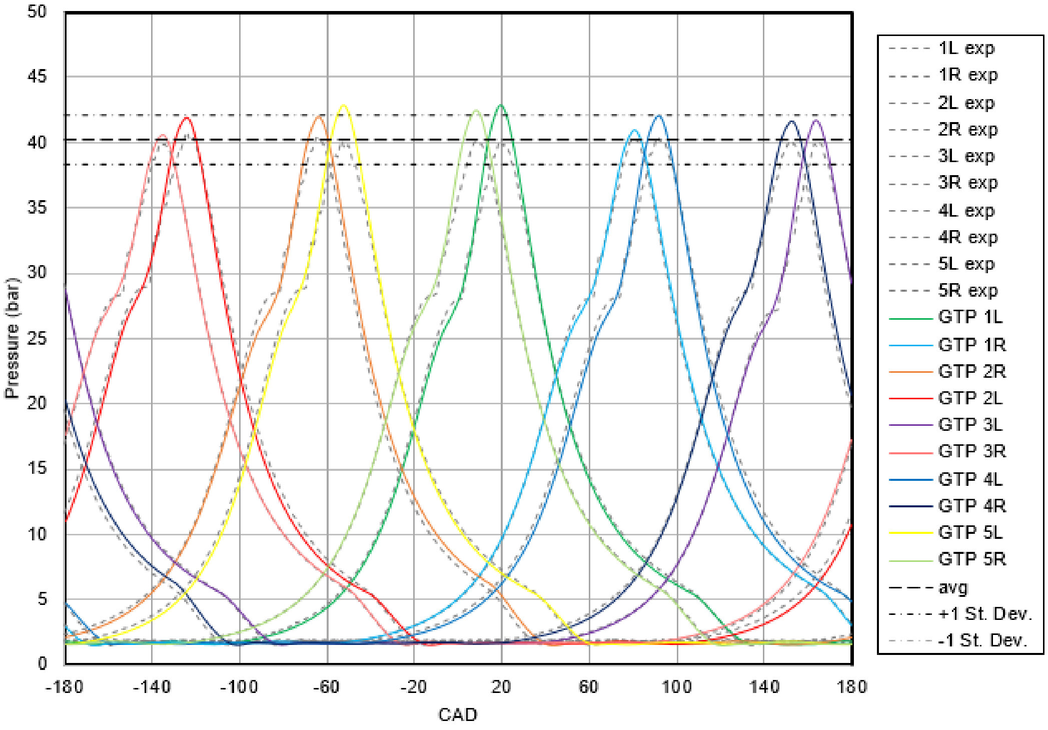

Figure 32: Pressure trace comparing simulation of prechambered model to experimental case over one flywheel revolution for Run 13

Run 13 shows significantly lower compression pressures. In an attempt to correct for this, the cylinder wall temperatures were increased by 100 K. However, this is not completely solve the issue, potentially because the air manifold pressure was much lower than expected. More tuning will be required to understand and correct for this.

7. SUGGESTIONS AND FUTURE WORK

It is planned to use the developed simulation to study how natural gas composition affects engine performance, efficiency, and emissions. This will require selecting the target variables of interest such as NO_x or other emissions production, peak combustion pressure, IMEP, etc. and which engine operating variables to change such as fuel flow, ignition timing, etc. The development of this test matrix is left for the next researcher.

Suggestions for improvement are as follows:

1. The discrepancy between the simulated and experimental pressures in the compression and power stroke could be due to the heat transfer model. While the Woschni model is commonly used, it has been shown to under-predict heat transfer for lean operating conditions.

2. If there is need to study a larger range of natural gas mixtures or to include hydrocarbons heavier than C5, then it would be straightforward to implement a larger chemical mechanism in to the Cantera code to calculate the laminar flame speed and ignition delay. Care should be taken when selecting the mechanism because computational time increases exponentially as the mechanism size increases.

3. For a more robust engine model and to improve the validation process, the engine, or the same engine at a different location, should be tested during a variable fuel composition event.

8. SUMMARY AND CONCLUSION

In this project, a full-scale engine simulation of a Cooper-Bessemer GMWH-10C was developed that included actual cylinder-level geometry of the piston motion and port timings in addition to a predictive combustion model that is able to calculate laminar flame speed from the fuel mixture.

The development of the piston kinematics used actual geometry of the V-configuration engine with an articulated crank. Due to the hinge-pin offset from the crankshaft, the power pistons have a different motion profile depending on which side of the engine the piston is relative to the compressor. This was shown to affect the port timings as much as 10 CAD, directly affecting the cylinder gas scavenging process

The chemical kinetics modeling used natural gas mixtures of alkanes from methane to pentane at a range of temperatures, pressures, equivalence ratios, and residual fractions to develop correlations that relate these variables to laminar flame speed and ignition delay. The laminar flame speed equation was implemented into the predictive combustion model, but the ignition delay equation was not deemed a good fit and is let for future refinement and implementation.

The engine model was verified against a range of experimental test conditions. In the future, it can be used to analyze how engine performance is affected by different fuels, and ultimately develop engine control schemes for implementation in the field.

REFERENCES

[1] J. Hedrick and T. Jacobs, "A review of variable natural gas composition, effects, and control methods for reliable combustion in lean burn two-stroke engines," *Pipeline Research Council International*, 2015.

[2] J. Heywood, Internal Combustion Engine Fundamentals, McGraw-Hill Education, 1988.

[3] E. R. Braziel, The Domino Effect: How the Shale Revolution is Transforming Energy Markets, Industries, and Economics, Houston: NTA Press, 2016.

[4] U.S. Energy Information Administration, "Today In Energy: The United States Exported More Natural Gas Than It Imported In 2017," U.S. Energy Information Administration, 19 March 2018. [Online]. Available: https://www.eia.gov/todayinenergy/detail.php?id=35392.

[5] K. Bullin and P. Krouskop, "Compositional Variety Complicates Processing Plans for US Shale Gas," *Oil & Gas Journal*, vol. 107, no. 10, pp. 50 - 55, 2009.

[6] U.S. Energy Information Administration, "Shale Gas and Oil Plays, North America," U.S. Energy Information Administration, May 2011. [Online]. Available: https://www.eia.gov/analysis/studies/usshalegas/.

[7] U.S. Energy Information Administration, "U.S. Natural Gas Pipeline Compressor Stations Illustration," U.S. Energy Information Administration, 2008. [Online]. Available: https://www.eia.gov/naturalgas/archive/analysis_publications/ngpipeline/compressorMap.html.

[8] "About U.S. Natural Gas Pipelines," June 2007. [Online]. Available: https://www.eia.gov/naturalgas/archive/analysis_publications/ngpipeline/index.html. [Accessed April 2018].

[9] M. Foss, "Interstate Natural Gas -- Quality Specifications and Interchangeability," in *Center for Energy Economics*, 2004.

[10] NGC+ Interchangeability Work Group, "White Paper on Natural Gas Interchangeability and Non-Combustion End Use," 2005.

[11] "Policy Statement on Provisions Governing Natural Gas Quality and Interchangeability in Interstate Natural Gas Pipeline Company Tariffs," U.S. Federal Energy Regulatory Commission, 2006.

[12] D. George and E. Bowles, "Shale Gas Measurement and Associated Issues," *Pipeline & Gas Journal*, vol. 238, no. 7, 2011.

[13] Advanced Engine Technologies Corporation, "Pipeline engine emissions control roadmap: Technology pathways to cost-effective year 2010 reciprocating engine emissions compliance," Pipeline Research Council International, 2005.

[14] C. Fletcher, C. Potter and G. Hutcherson, "Revitalization of the GMW Engine Family," in *Gas Machinery Conference*, Colorado Springs, 2000.

[15] J. Adair, A. Kirkpatrick, D. Olsen and H. Gitano-Briggs, "Simulation of the airflow characteristics of a two-stroke natural gas engine with an articulated crank," *ASME Internal Combustion Engine Division Spring Technical Conference*, Vols. ICES2003-552, 2003.

[16] K. Evans, D. Olsen and B. Willson, "Fuel and ignition control methodologies for engines with articulated connecting rods," *Int. J. Engine Res.*, vol. 6, pp. 207-214, 2005.

[17] D. Olsen, G. Hutcherson, B. Willson and C. Mitchell, "Development of the Traver Gas Method for Large Bore Natural Gas Engines -- Part I: Method Validation," *Journal of Engineering for Gas Turbines and Power*, vol. 124, pp. 678 - 685, 2002.

[18] D. Olsen, G. Hutcherson, B. Willson and C. Mitchell, "Development of the Traver Gas Method for Large Bore Natural Gas Engines -- Part II: Measurement of Scavenging Parameters," *Journal of Engineering for Gas Turbines and Power*, vol. 124, pp. 686 - 694, 2002.

[19] D. Olsen and A. Kirkpatrick, "Experimental Examination of Prechamber Heat Release in a Large Bore Natural Gas Engine," *Journal of Engineering for Gas Turbines and Power*, 2008.

[20] D. Olsen, J. Adair and B. Willson, "Precombustion Chamber Design and Performance Studies for a Large Bore Natural Gas Engine," in *ASME Internal Combustion Engine Division Spring Technical Conference* , 2005.

[21] M. Ruter, D. Olsen, M. Scotto and M. Perna, "Performance of a Large Bore Natural Gas Engine with Reformed Natural Gas Prechamber Fueling," in *ASME Internal Combustion Engine Division Fall Technical Conference*, San Antonio, 2010.

[22] A. Kirkpatrick, G. Kim and D. Olsen, "CFD Modeling of the Performance of a Prechamber for Use in a Large Bore Natural Gas Engine," in *ASME Internal Combustion Engine Division Spring Technical Conference*, Chicago, 2005.

[23] Z. Dursunkaya and R. Keribar, "Simulation of Secondary Dynamics of Articulated and Conventional Piston Assemblies," in *SAE International Congress & Exposition*, Detroit, 1992.

[24] J. Rojewski, "Optimization of Combustion Processes in Industrial Gas Engines," Doctoral Dissertation, Poznan University of Technology, Poznan, 2014.

[25] W. Liss, W. Thrasher, G. Steinmetz, P. Chowdiah and A. Attari, "Variability of Natural Gas Composition in Select Major Metropolitan Areas. Final Report, August 1990 - February 1992," *American Gas Association Labs, Cleveland*, 1992.

[26] R. Matthews, J. Chiu and D. Hilden, "CNG Compositions in Texas and the Effects of Composition on Emissions, Fuel Economy, and Drivability of NGVs," in *SAE International Fall Fuels & Lubricants Meeting & Exposition*, San Antonio, 1996.

[27] L. L. C. Silva and M. Zulauf, "Variability of Natural Gas Composition in Brazil," in *SAE International Fall Fuels & Lubrications Meeting & Exposition*, Tulsa, 1997.

[28] T. Lindgren, "Change of Gas Quality: A Case Study from Denmark," in *European Gas Technology Conference*, Paris, 2013.

[29] J. Leicher, A. Giese, K. Görner, M. Werschy, H. Krause and H. Dörr, "Natural Gas Quality Fluctuations -- Surveys and Statistics on the Situation in Germany," *Energy Procedia,* vol. 120, pp. 165 - 172, 2017.

[30] X. Li, "Natural Gas in China: A Regional Analysis," in *The Oxford Institute for Energy Studies*, 2015.

[31] Bakshi, V. (ed.), Shale Gas: A Practitioner's Guide to Shale Gas and Other Unconventional Resources, London: Globe Business Publishing Ltd., 2012.

[32] C. Freeman, G. Moridis and T. Blasingame, "Modeling and Performance Interpretation of Flowing Gas Composition Changes in Shale Gas Wells with Complex Fractures," in *International Petroleum Technology Conference*, Beijing, 2013.

[33] L. Zhang, D. Li, L. Wang and D. Lu, "Simulation of Gas Transport in Tight/Shale Gas Reservoirs by a Multicomponent Model Based on PEBI Grid," *Journal of Chemistry,* vol. 2015, 2014.

[34] K. Schafer and S. Fletcher, "High BTU Fuel Gas from the Marcellus Shale and how it Affects Emissions and Peak Firing Pressures," in *Gas Machinery Conference*, 2010.

[35] G. Choquette, "Analysis and Estimation of Stoichiometric Air-Fuel Ratio and Methane Number for Natural Gas," in *Gas Machinery Conference,* Nashville, 2014.

[36] S. Turns, An Introduction to Combustion: Concepts and Applications, McGraw-Hill, 1996.

[37] A. Liñán and F. Williams, Fundamental Aspects of Combustion, New York: Oxford University Press, Inc., 1993.

[38] M. Metghalchi and J. Keck, "Burning velocities of mixures of air with methanol, isooctane, and indolene at high pressure and temperature," *Combustion and Flame,* pp. 191-210, 1982.

[39] S. Liao, D. Jiang and Q. Cheng, "Determination of laminar burning velocities for natural gas," *Fuel 83,* pp. 1247-1250, 2004.

[40] J. Hernandez, M. Lapuerta and C. Serrano, "Estimation of the laminar flame speed of producer gas from biomass gasification," *Energy & Fuels 19,* pp. 2172-2178, 2005.

[41] Gamma Technologies, "GT-SUITE: Engine Performance Application Manual," Gamma Technologies LLC, Westmont, 2017.

[42] E. Sher and Y. Hacohen, "Ignition Delay and Combustion Duration in H2-Enriched Gasoline SI Engines," *Combustion Science and Technology*, vol. 65, pp. 263 - 275, 1989.

[43] J. Livengood and P. Wu, "Correlation of autoignition phenomena in internal combustion engines and rapid compression machines," *Internat. Symposium on Combustion 5.1*, 1955.

[44] J. Hedrick and T. Jacobs, "Variable NG composition effects in LB 2S compressor engines Phase II -- prediction enhancements," Pipeline Research Council International, 2016.

[45] J. Hedrick and T. Jacobs, "Variable natural gas composition effects in lean burn two-stroke compressor engines Phase I -- engine response final report," Pipeline Research Council International, 2015.

[46] D. Goodwin, "An Open-Source, Extensible Software Suite for CVD Process Simulation," in *California Institute of Technology*, Pasadena, 2003.

[47] G. Woschni, "A Universally Applicable Equation for the Instantaneous Heat Transfer Coefficient in the Internal Combustion Engine," *SAE Paper 670931*, vol. 76, 1967.

[48] B. Hopkinson, "The Charging of Two-Cycle Internal Combustion Engines," *Transactions of the North East Coast Institution of Engineers and Shipbuilders*, vol. 30, 1914.

[49] G. Blair, Design and Simulation of Two-Stroke Engines, Warrendale: Society of Automotive Engineers, Inc., 1996.

[50] S. Chen and P. Flynn, "Development of a Single Cylinder Compression Ignition Research Engine," in *National Powerplant and Transportation Meetings, SAE Paper 650733*, Cleveland, 1965.

[51] C. E. C. Alvarez, G. E. Couto, V. R. Roso, A. B. Thiriet and R. M. Valle, "A Review of Prechamber Ignition Systems as Lean Combustion Technology for SI Engines," *Applied Thermal Engineering,* vol. 128, pp. 107 - 120, 2018.

[52] H. Mathews, G. Beshouri, B. Goffin and G. Choquette, "Trapped Equivalence Ratio for Air Fuel Ratio Control - Review and Update," in *Gas Machinery Conference,* Pittsburgh, 2017.

[53] K. Fieseler, T. Jacobs and M. Patterson, "Kinematics of an Articulated Connecting Rod and Its Effect on Simulated Compression Pressures and Port Timings," *Journal of Engineering for Gas Turbines and Power,* vol. 140, no. 9, 2018.

[54] D. Healy, D. Kalitan, C. Aul, E. Petersen, G. Bourque and H. Curran, "Oxidation of C1 - C5 quinternary natural gas mixtures at high pressures," *Energy & Fuels*, vol. 24, pp. 1521-1528, 2010.

[55] G. Beshouri, D. Lepley, L. Tozzi and E. Sotiropoulou, "A New Look at the Design and Operation of Screw-In Pre Combustion Chambers," in *Gas Machinery Conference*, 2016.

[56] G. Bourque, D. Healy, H. Curran, C. Zinner, D. Kalitan, J. de Vries, C. Aul and E. Petersen, "Ignition and flame speed kinetics of two natural gas blends with high levels of heavier hydrocarbons," *Journal of Engineering for Gas Turbines adn Power,* vol. 132, 2010.

[57] C. Aul, W. Metcalfe, S. Burke, H. Curran and E. Petersen, "Ignition and kinetic modeling of methane and ethane fuel blends with oxygen: a design of experiments approach," *Combustion and Flame,* vol. 160, pp. 1153-1167, 2013.

[58] "Major Legislative and Regulatory Actions: Natural Gas Act of 1938," U.S. Energy Information Administration, 2009. [Online]. Available: https://www.eia.gov/oil_gas/natural_gas/analysis_publications/ngmajorleg/ngact1938.html. [Accessed May 2018].

[59] W. Liss, "Fuel Issues for Gas Engines an NGVs," in *Windsor Workshop on Alternative Fuels*, 1993.

[60] C. Freeman, G. Moridis, G. Michael and T. Blasingame, "Measurement, Modeling, and Diagnostics of Flowing Gas Composition Changes in Shale Gas Wells," in *SPE Latin American and Carribbean Petroleum Engineering Conference*, Mexico City, 2012.

[61] T. Morel and R. Keribar, "A Model for Predicting Spatially and Time Resolved Convective Heat Transfer in Bowl-in-Piston Combustion Chambers," in *SAE Technical Paper 850204*, 1985.

[62] S. Hires, R. Tabaczynski and J. Novak, "The Prediction of Ignition Delay and Combustion Intervals for a Homogenous Charge, Spark Ignition Engine," *SAE Paper 780232*, pp. 1053 - 1067, 1979.

APPENDICES

A.1 LFS and ID Cantera Code Verification

A study conducted by Bourque, et al. tested the laminar flame speed and ignition delay of two natural gas mixtures consisting of methane, ethane, propane, butane, and pentane. [56] Due to the high amounts of heavier hydrocarbons, this data was chosen to validate the Cantera model. The mixture compositions are shown in Table 15.

Table 15: Fractional composition of two natural gas fuel blends from [56]

Species	NG2	NG3
CH_4	0.8128	0.6250
C_2H_6	0.1000	0.2000
C_3H_8	0.0500	0.1000
n-C_4H_{10}	0.0250	0.0500
n-C_5H_{12}	0.0125	0.0250

Using Cantera, these two mixtures were tested at an initial pressure of 1 atm and an initial pressure of 298 K at equivalence ratios from 0.7 to 1.3. The comparison of Bourque, et al.'s experiment [56] and the simulation are shown in Figure 33 and Figure 34. Additionally, NG3 was tested at a range of pressures from 1 to 4 atm at an initial temperature of 298 K. The results of this sweep are shown in Figure 35.

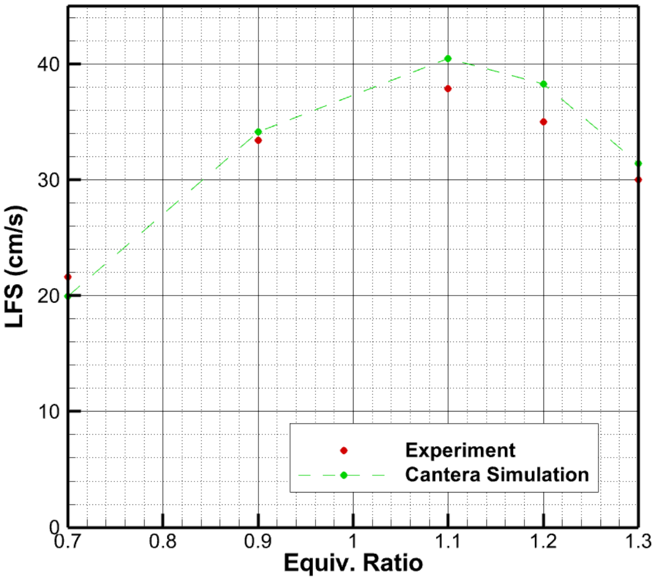

Figure 33: NG2 mixture from Bourque, et al. at 1 atm and 298 K initial conditions compared to the Cantera calculation

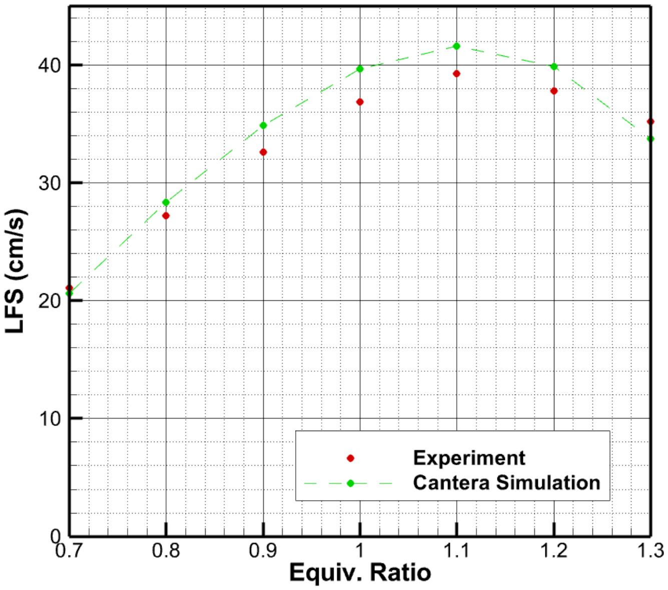

Figure 34: NG3 mixture from Bourque, et al. at 1 atm and 298 K initial conditions compared to the Cantera calculation

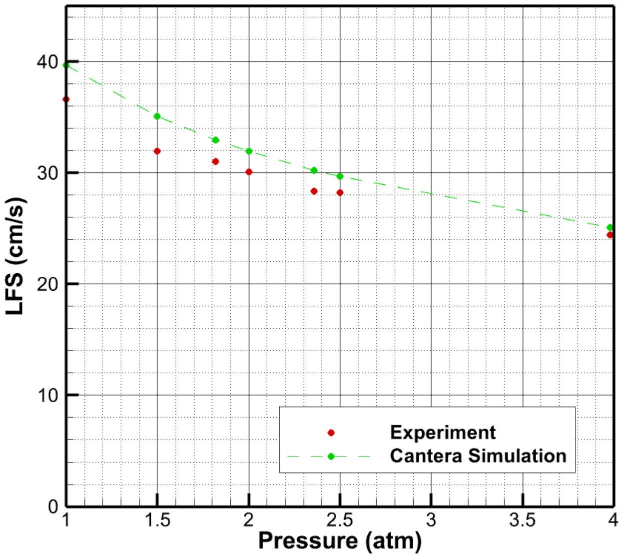

Figure 35: NG3 mixture from Bourque, et al. at stoichiometric and 298 K initial conditions compared to Cantera calculation

Overall, there is a good match between the simulation and experimental data. The worst match is shown in Figure 33 at an equivalence ratio of 1.2 when the difference is 9.3%. All the other points have a smaller percent difference.

There is inherent uncertainty in experimental values. For the LFS, the largest source of error is in the initial temperature which is 298 ± 1 K. The values between the experimental data and calculation are close and follow similar trends. Therefore, the Cantera code and chemical mechanism are functioning properly for the LFS calculations.

For ignition delay, a study by Aul, et al. [57] was chosen to compare the data sets because it used a larger test matrix. A variety of methane/ethane blends were tested at a large range of dilutions, equivalence ratios, and initial pressures.

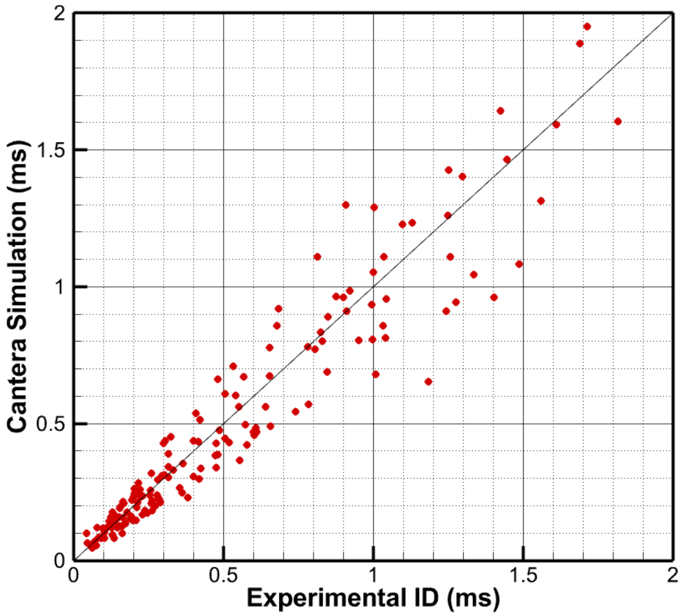

Figure 36: All 180 data points tested by Aul, et al. compared to Cantera

When ignition delay is experimentally determined, there is inherent uncertainty in the initial conditions. Perhaps the biggest source of uncertainty is in the measurement of the shockwave speed which affects the initial temperature of the mixture. In turn, this could cause a discrepancy between the experimentally reported value for initial temperature and the actual value, leading to the scatter shown in the figure. Even so, there is good agreement between the experimental and calculated values.

Overall, these preliminary trial studies show the mechanism and Cantera code are functioning properly, and they can be used to calculate the LFS and ID for the mixtures and conditions of interest.

A.2 GT-Power Model

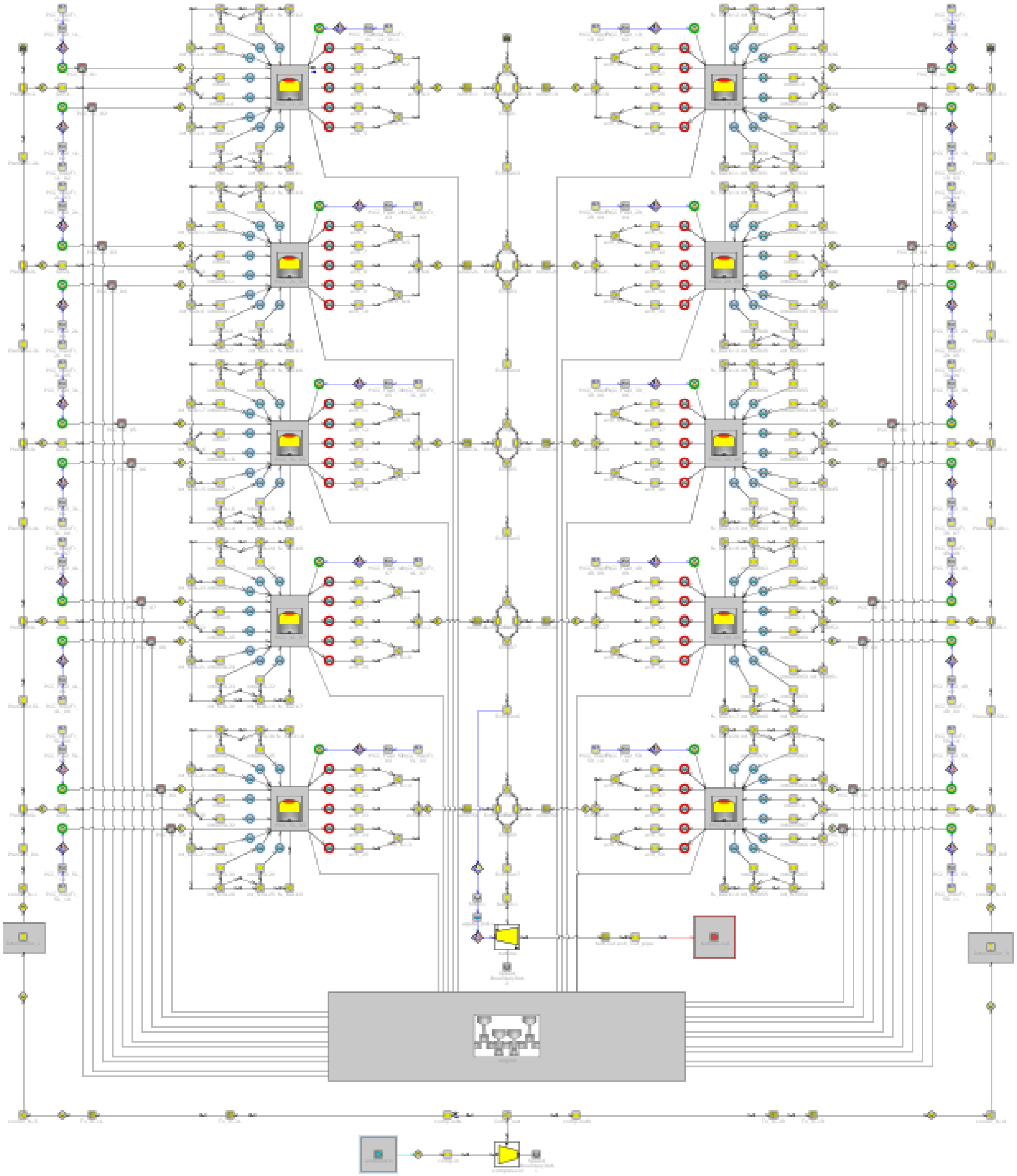

Figure 37: GT-Power model of the engine

A.3 Pressure vs. Crank Angle Plots

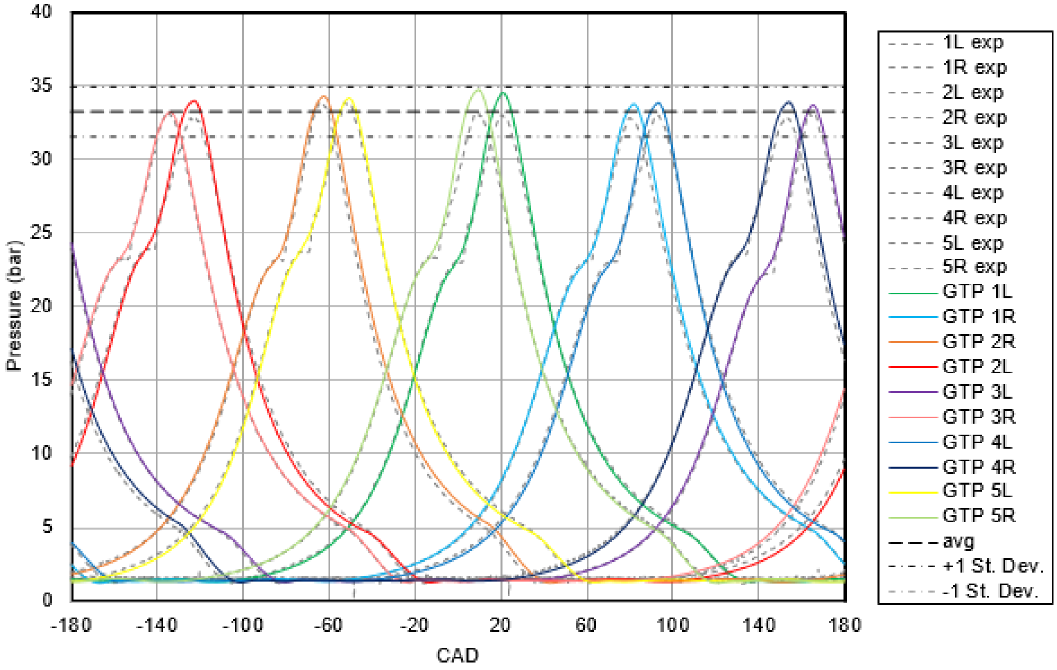

Figure 38: Pressure trace comparing simulation of prechambered model to experimental case over one flywheel revolution for Run 1

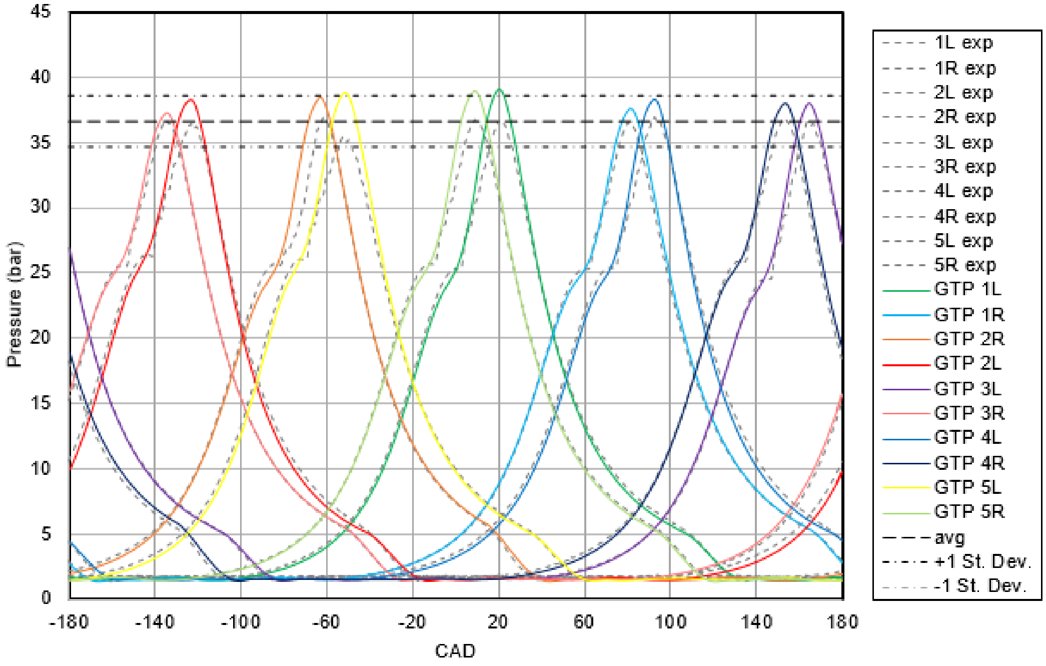

Figure 39: Pressure trace comparing simulation of prechambered model to experimental case over one flywheel revolution for Run 2

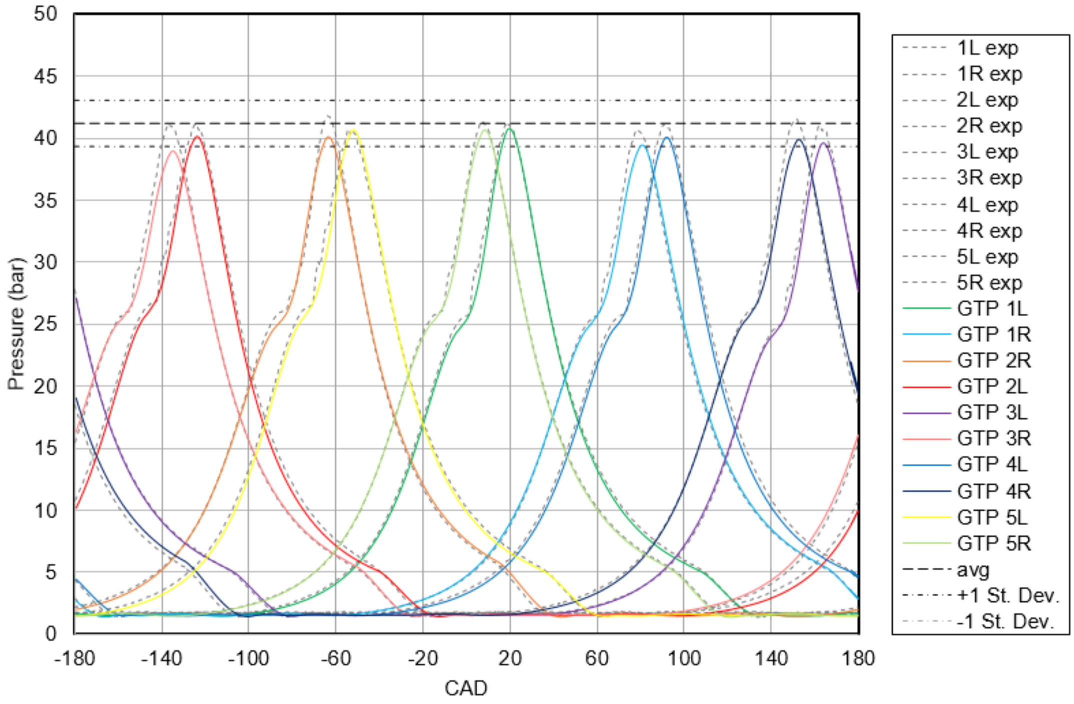

Figure 40: Pressure trace comparing simulation of prechambered model to experimental case over one flywheel revolution for Run 6

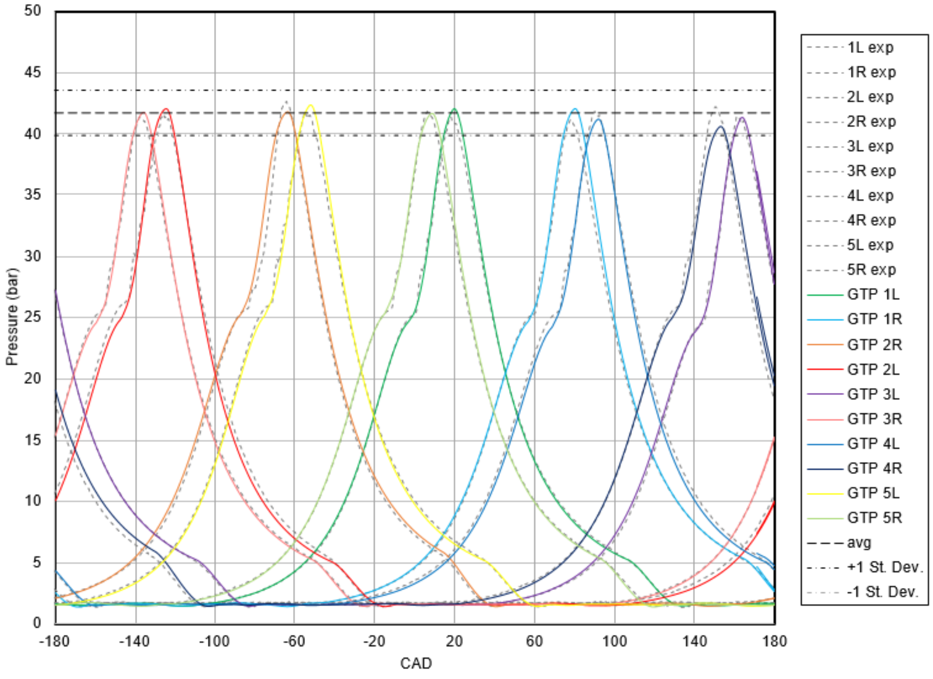

Figure 41: Pressure trace comparing simulation of prechambered model to experimental case over one flywheel revolution for Run 7

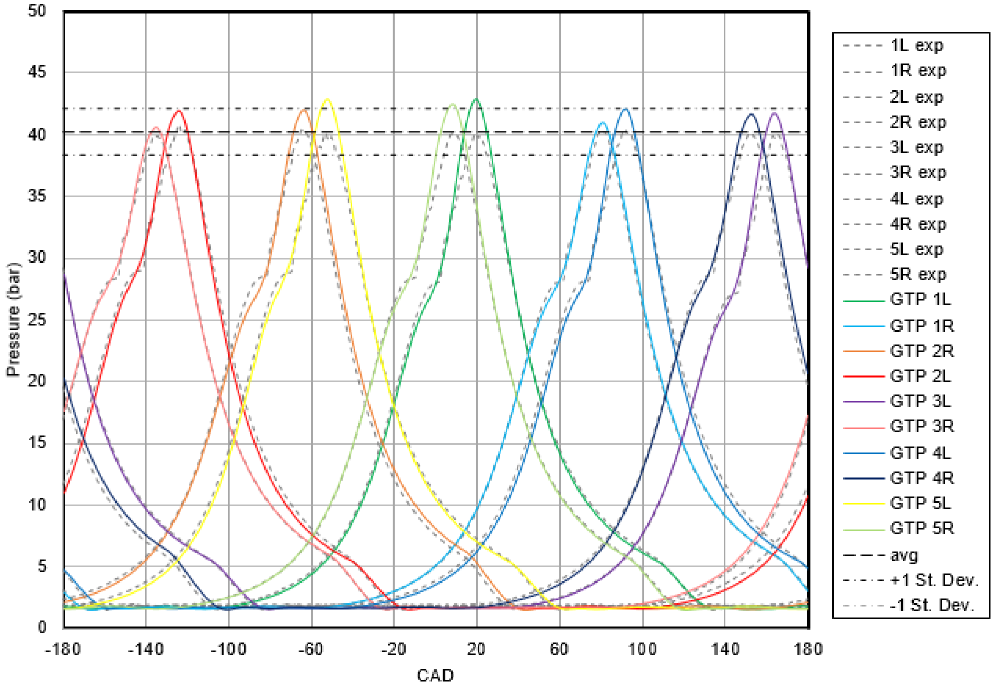

Figure 42: Pressure trace comparing simulation of prechambered model to experimental case over one flywheel revolution for Run 12

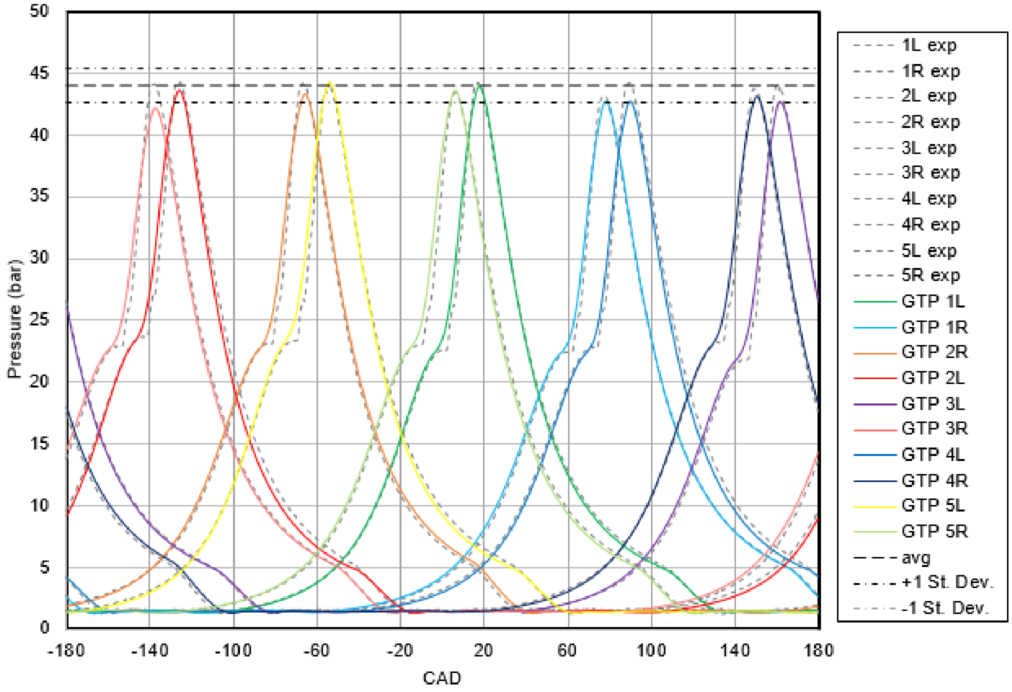

Figure 43: Pressure trace comparing simulation of prechambered model to experimental case over one flywheel revolution for Run 16

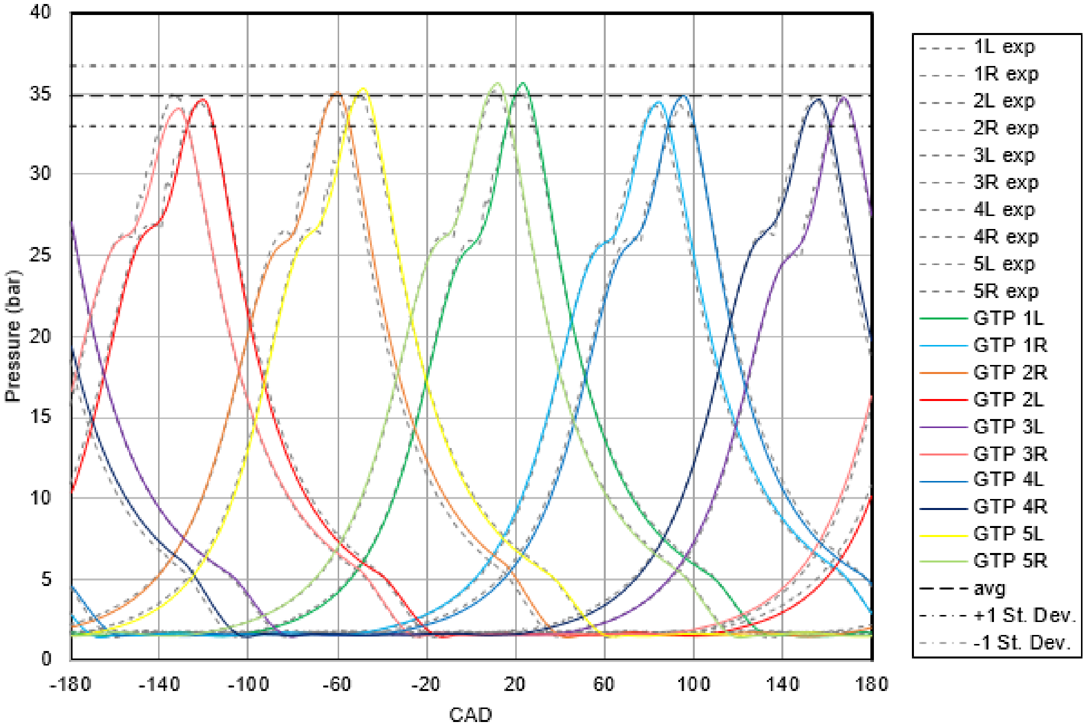

Figure 44: Pressure trace comparing simulation of prechambered model to experimental case over one flywheel revolution for Run 17